

AD-A130 990

MICRO-OPTIC GYRO TECHNOLOGY(U) NORTHROP CORP NORWOOD MA 1/1  
PRECISION PRODUCTS DIV J M CONNORS ET AL JAN 83  
PPD-E-83-10589 DAAH01-81-C-B138

UNCLASSIFIED

F/G 17/7

NI

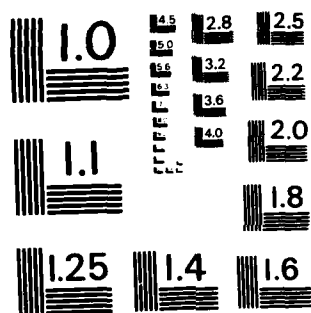
END

DATE

FILED

6 83

DTIC



MICROCOPY RESOLUTION TEST CHART  
NATIONAL BUREAU OF STANDARDS - 1963 - A

ADA 130996

DTIC FILE COPY

DISTRIBUTION STATEMENT A

Approved for public release;  
Distribution Unlimited

DTIC  
ELECTE  
AUG 2 1983  
S B

Final Report  
MICRO-OPTIC GYRO TECHNOLOGY  
Contract DAAH-01-81-C-8138  
Report No. PPD-E-83-10589

January 1983

**NORTHROP**  
Precision Products  
Division

83 07 26 . 112

Final Report  
MICRO-OPTIC GYRO TECHNOLOGY  
(Contract DAAH-01-81-C-8138)

Submitted to  
US Army Missile Command  
Guidance and Control Directorate  
Redstone Arsenal  
Huntsville, AL 35809

Report No. PPD-E-83-10589

January 1983

*JM Connors*

J. M. Connors  
Engineer

*A W Lawrence*

A. W. Lawrence  
Section Manager  
Component Development

*JR Haavisto*

J. R. Haavisto, PhD  
Senior Member, Technical Staff

DTIC  
ELECTE  
S AUG 2 1983 D  
B

**DISTRIBUTION STATEMENT A**

Approved for public release  
Distribution Unlimited

NORTHROP CORPORATION  
Precision Products Division  
Norwood, Massachusetts 02062

## Table of Contents

	Page
I. Introduction	1-1
1.1 Description of the Micro-Optic Gyro	1-1
1.2 History of the MOG Program	1-4
II. Achievement of Technical Requirements	2-1
III. Frequency Shifter Design	3-1
3.1 Summary of Design	3-1
3.2 Design Considerations	3-3
3.3 Acousto-Optic Interaction	3-5
3.4 Horn Design	3-7
3.5 Determining Waveguide Horn Width	3-9
3.6 Integration Approach	3-11
IV. Horn Waveguide Fabrication	4-1
V. LiNbO <sub>3</sub> -Polymer Coupling	5-1
VI. SAW Device Fabrication	6-1
VII. Conclusions and Recommendations	7-1

### Appendix A. Tapered Horn Experiment

### Appendix B. Diffused Waveguide Parameters



Accession For	
NTIS GRA&I	<input checked="" type="checkbox"/>
DTIC TAB	<input type="checkbox"/>
Unannounced	<input type="checkbox"/>
Justification	
<b>PER LETTER</b>	
By _____	
Distribution/ _____	
Availability Codes	
Dist	Avail and/or Special
<b>A</b>	

## Section I

### INTRODUCTION

#### 1.1 DESCRIPTION OF THE MICRO-OPTIC GYRO

This final technical report covers the work performed under Contract DAAH-01-81-C-B138 by Northrop's Precision Products Division (PPD) in Norwood, MA.

Phase I objectives were:

- Review the literature relevant to the design and fabrication of thin-film frequency shifters and integrated waveguide/frequency shifters

- Produce a design for integrated waveguide/frequency shifters applicable to the passive ring resonator (PARR) micro-optic gyro.

Phase II objectives were to:

- Perform the technology tasks necessary for integration

- Fabricate shifters

- Perform integration experiments

The final version of Northrop's micro-optic gyro (MOG) will consist of thin-film devices integrated on a common substrate. We have previously demonstrated that it is possible to construct a resonant cavity from thin-film waveguides. The current effort is to integrate thin-film frequency shifters with these waveguide resonators. This section describes the operation of the MOG and presents a brief history of the program.

The results of the program tasks are summarized in Section II.

Section III summarizes Phase I results. The technology experiments are discussed in Sections IV (Horn Waveguide Fabrication), V, (LiNbO<sub>3</sub>-Polymer Coupling), and VI (SAW Device Fabrication).

The MOG is an integrated optics embodiment of the Passive Ring Resonator (PARR) gyro. Rotation rate ( $\Omega$ ) is determined by the change in resonant frequency of a waveguide ring. Under rotation, light traveling in opposite directions in the ring sees an effective difference in perimeter and thus a difference in resonant frequency given by the Sagnac effect as:

$$\Delta f = S\Omega$$

where the scale factor is given by:

$$S = (d/n\lambda)$$

where:  $d$  = diameter of ring  
 $n$  = effective index of waveguide  
 $\lambda$  = free space wavelength of light used

The resonant frequency of the ring is determined by using an external laser source to excite the resonant frequency in each direction. A schematic configuration of the MOG is shown in figure 1-1.

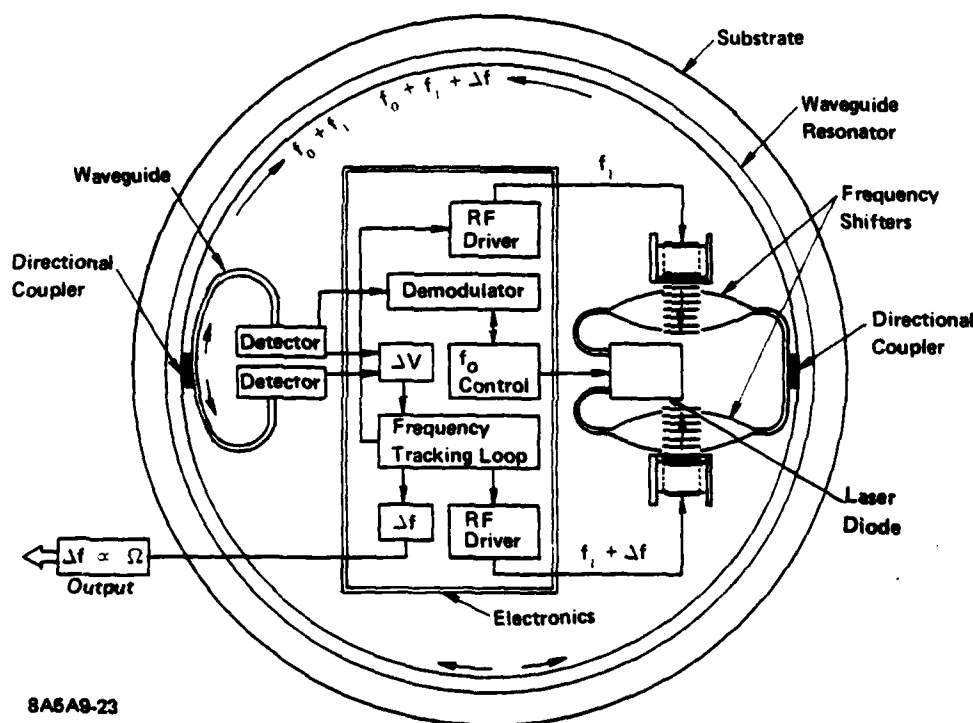


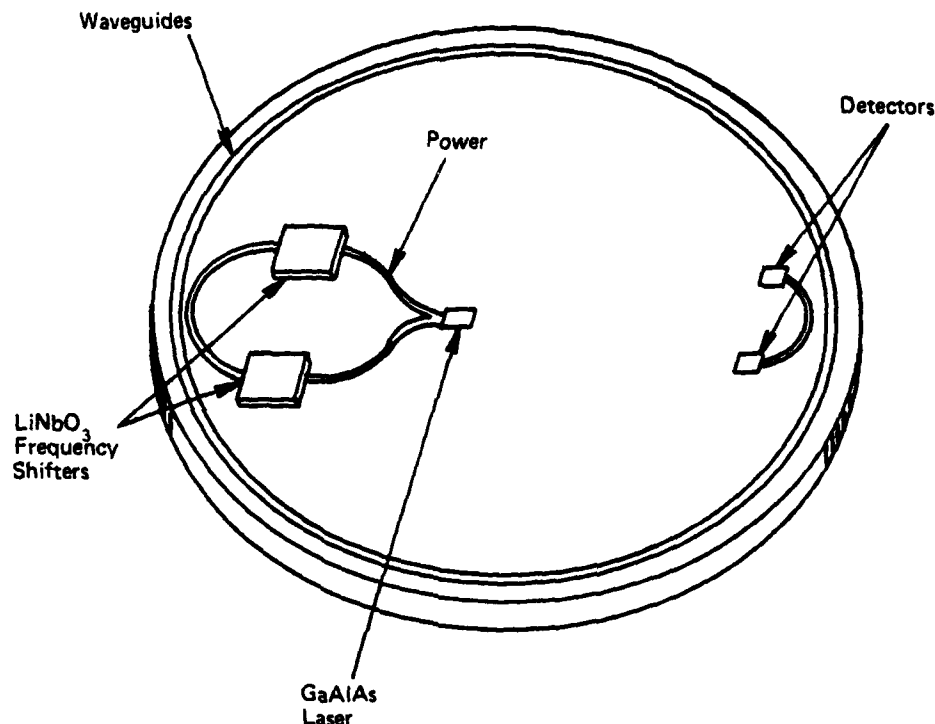
Figure 1-1. Schematic Representation of Micro-Optic Laser Gyro

The output of a laser diode is coupled into a thin-film waveguide and power splitter which provides two identical inputs to separately controlled thin-film frequency shifters. The output of the frequency shifters is coupled into the resonator through a directional coupler, one wave traveling clockwise (CW) in the ring, the other counterclockwise (CCW). The light traveling in the waveguide is sampled by a second directional coupler. The output from each direction goes to a detector which generates an electrical signal proportional to the intensity of the light. The intensity of the light traveling in either direction is at maximum when the frequency of the light is a resonant frequency. The output of one direction (CW) is maintained at maximum by continuously tuning the output frequency ( $f_0$ ) of the laser; the resonant frequency is actually  $f_0 + f_1$  where  $f_1$  is the fixed frequency shift supplied by the CW frequency shifter. The other direction is maintained on resonance by providing a signal  $f_1 + \Delta f$  to the CCW frequency shifter. Thus both directions are maintained on resonance and  $\Delta f$  represents the difference in resonant frequencies between the two directions. In the absence of rotations,  $\Delta f = 0$ . Under rotation, the frequency difference required to maintain the CCW direction on resonance is a direct measure of the rotation rate with the scale factor given above.

Northrop plans to meet the low cost requirements for tactical strapdown applications by using integrated optics as the basis for fabricating the MOG. The gyros will be constructed on a common substrate with a semiconductor laser and thin-film frequency shifters rigidly connected by a polymer waveguide structure (figure 1-2). The ideal approach would be to deposit thin-film frequency shifters and resonator waveguides on a common quartz substrate. This would minimize fabrication requirements, and greatly simplify integration requirements. By interconnecting the devices with waveguides, the alignment is fixed and the environmental sensitivities prevalent in conventional optical devices are eliminated. Eventually all sensor functions can be combined on a single substrate: gyro optics, gyro electronics, accelerometer, compensation sensors, and signal processing.

In the prototype MOG gyro now under development, the laser is a single-mode, gallium aluminum arsenide (GaAlAs) semiconductor laser. The output of the laser is coupled into a single-mode channel waveguide, which is configured to split the output into two channels. These waveguide channels direct the light into the lithium niobate ( $\text{LiNbO}_3$ ) frequency shifters, which Doppler shift the light with a surface acoustic wave (SAW) traveling on the  $\text{LiNbO}_3$  crystal. The amount of frequency shift is precisely the same as the frequency of the SAW which is generated by an RF signal applied to a set of metal transducer fingers on the crystal surface.





21M2G-2

Figure 1-2. Configuration of the Prototype Micro-Optic Gyro

## 1.2 HISTORY OF THE MOG PROGRAM

The MOG has been under development at Northrop since 1977, when the emergence of integrated optics raised the exciting possibility that a solid-state laser gyro might be practical. The disclosure of the PARR concept by Prof. Ezekiel at MIT in 1976 provided the ideal concept for integrated optics implementation; the ideal application seemed to be a low-cost strapdown gyro for tactical applications. The first task was to perform a feasibility study which would determine the relationship between gyro performance and the operating characteristics of the optical components and the electronics. The work, performed under contract to the US Navy in 1978, identified areas needed in component development that were questionable for providing 1 to 10°/hr performance. The key component is the waveguide resonator. As detailed in the final report under this contract,<sup>(1)</sup> the shot noise limited (SNL) sensitivity is set by the linewidth of the resonator and the signal-to-noise (S/N) ratio at the detector.

It was shown that the waveguide resonator must have total losses of less than 0.1 dB for 1°/hr performance, assuming a 10 cm diameter gyro with available input power of 1 mw and integration time of 1 second. At the time (1978), the best published losses for single-mode thin-film waveguides was 0.2 dB/cm, nearly two orders of magnitude above that required. Thus a prime task by PPD was to attempt to develop a low-loss waveguide resonator suitable for low-cost, high-volume production. Much of this development work was funded under two contracts jointly sponsored by MICOM, Huntsville and AFAL, Eglin AFB, from 1979 through 1982.<sup>(2,3)</sup> During this period, techniques were established at PPD for fabricating the resonators using low-loss waveguides. The losses achieved by PPD, <0.02 dB/cm, are the lowest losses in single-mode waveguides to date. In fact, these remain the only waveguides reported with losses less than 0.2 dB/cm.

Reduction in waveguide losses resulted in current losses measured in the 0.01 to 0.02 dB/cm range. The resonator improvement program is continuing under PPD IRAD funding and further improvements are expected. While the goal of 0.005 dB/cm has not been achieved the current waveguide resonators made at PPD are suitable for operation in the 1 to 10°/hr range. During the course of the MOG program, several hundred resonators have been made for evaluation. Extensive studies have been performed on the waveguide properties influencing resonator operation, and a paper was published.<sup>(4)</sup> Tests conducted on resonators included aging, closed-loop behavior, temperature effects, polarization effects, and backscattering effects. Light has been coupled into resonators in both directions simultaneously and independent resonant behavior observed. No other thin-film waveguide resonator has been reported.

The original studies indicated that the frequency shifter requirements for the MOG were quite modest and easily attained by existing devices. The 1 MHz bandwidth requirement, frequency stability, shifting efficiency, and optical transmission could be easily met by frequency shifters based on lithium niobate crystals. Accordingly, based on MOG requirements and published results in the technical literature, a frequency shifter was designed and fabricated by Northrop Research and Technology Center (NRTC) under PPD IRAD funding. The device was tested successfully by NRTC and PPD. Then the techniques were transferred to PPD. A successful PPD device was demonstrated in August 1982.

The effort to integrate the components into a gyro began in 1981. Most of the effort in integrating the LiNbO<sub>3</sub> frequency shifters with polymer waveguides has been performed at PPD under this contract. As a part of this effort, frequency shifters have been made and tested at PPD; waveguides for connecting the frequency shifter with the single-mode waveguides have been designed and fabricated; and frequency shifter-resonator integration begun. The results are summarized in the following sections. While PPD has not successfully demonstrated integration, recent publications describe integration techniques for frequency shifter-waveguide and laser-waveguide coupling with results in excess of requirements for the MOG.

## Section II

### ACHIEVEMENT OF TECHNICAL REQUIREMENTS

Technical Requirement No. R-0070 defined the scope of work for this contract as follows.

#### Section I: General

The scope of work under this contract consists of the design of frequency shifters, technology experiments, the fabrication and evaluation of frequency shifters, and the integration and evaluation of frequency shifters with a waveguide resonator. The frequency shifters and waveguide resonator will become integral parts of a micro-optic laser gyro. This work will make use of the expertise acquired under Contracts DAAK40-79-C-0052 and DAAK40-79-C-0235.

#### Section II: Requirements

##### Phase I

##### 2.1 Design Frequency Shifter

2.1.1 The contractor shall design integrated thin-film frequency shifters.

- a. The frequency shifter will have a bandwidth approximately 2 MHz and a loss less than 1 dB.
- b. At the completion of this section, a report will be issued which will list the design criterion for producing a thin-film frequency shifter as well as all analysis that led to the particular design.

##### Phase II

##### 2.2 Technology Experiments

2.2.1 The contractor shall fabricate and evaluate horn waveguides for use in a micro-optic laser gyro.

- a. The horn design as well as the techniques used in fabricating the particular horn design will be reported.
- b. The horn waveguide will be evaluated for maximum frequency shifter efficiency and signal resolution.

2.2.2 The contractor shall optimize polymer guides to Ti-diffused LiNbO<sub>3</sub> guide coupling.

2.2.3 The contractor shall design and fabricate SAW chips in  $\text{LiNbO}_3$ .

- a. Design a Surface Acoustic Wave (SAW) frequency shifter that can be deposited in a  $\text{LiNbO}_3$  substrate. Sufficient numbers of the SAW chip will then be fabricated, deposited in the  $\text{LiNbO}_3$  substrate and evaluated for performance efficiency.

## 2.3 Shifter Fabrication Experiments

2.3.1 The contractor shall fabricate and evaluate half shifters and make necessary changes to achieve optimum performance.

2.3.2 The contractor shall fabricate and evaluate full shifter and make necessary changes to achieve optimum performance.

## 2.4 Integration Experiments

2.4.1 The contractor shall integrate a frequency shifter with a ring resonator and evaluate its performance.

Requirement 2.1, Phase I - Frequency Shifter Design - was completed on schedule and a final report submitted in December 1981. A summary of the results is presented in Section 3. A frequency shifter design and fabrication approach for a low-loss (<1 dB) and moderate bandwidth (>2 MHz) was established. The frequency shifters use lithium niobate waveguides and the integration with polymer waveguides uses step-etching and flip-chip coupling for high efficiency.

The technology experiments (Task 2.2) conducted under the contract included horn design, fabrication, and evaluation (2.2.1), polymer guide to Ti-diffused  $\text{LiNbO}_3$  guide coupling (2.2.2), and SAW chip fabrication and evaluation. Horns were made using both commercial masks and laser writing techniques. A double horn for use in tasks 2.3 and 2.4 was designed and fabricated. Coupling from polymer waveguides into in-diffused  $\text{LiNbO}_3$  waveguides was observed but the step etching of the  $\text{LiNbO}_3$  necessary to optimize bidirectional coupling efficiency was not satisfactorily completed. Masks for the SAW fabrication were obtained and photolithography techniques established. Frequency shifters were fabricated and efficiency of over 60 percent demonstrated. The frequency shifters met the requirements for use in tasks 2.3 and 2.4. Details of the work performed under these tasks are given in sections 4, 5 and 6.

The inability to step etch the  $\text{LiNbO}_3$  (using PPD and outside facilities) precluded the completion of tasks 2.3 and 2.4. The difficulties are described in detail in section 5.

# Section III

## FREQUENCY SHIFTER DESIGN

### 3.1 SUMMARY OF DESIGN

PPD's approach involves the hybridization of techniques which have been demonstrated separately, but never combined in a single device. The frequency shifter itself will be a guided-wave, surface-acoustic-wave Bragg cell, a device which is well known in the literature.<sup>5</sup> The Bragg cell will be physically attached to the quartz substrate, and the polymethylmethacrylate (PMMA) waveguide will be mated to the Bragg cell waveguide by the technique called "butt-end coupling."<sup>(5)</sup> An overall sketch of the device is shown in figure 3-1.

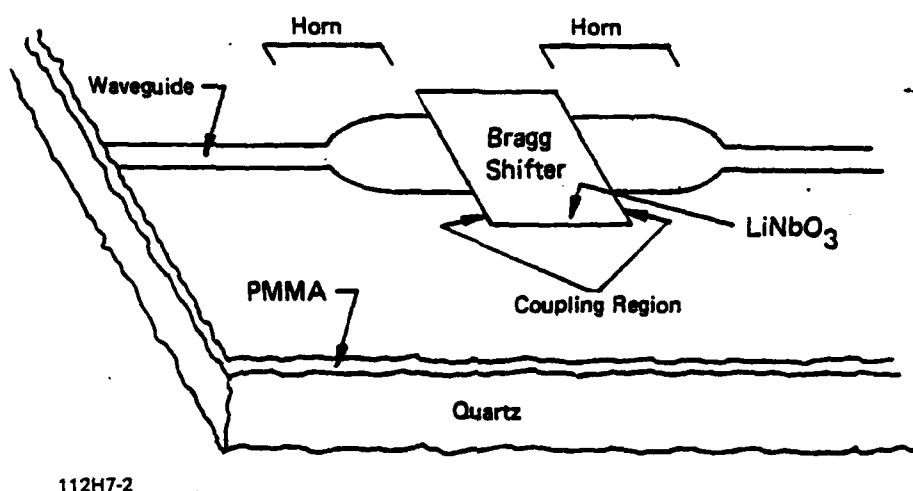


Figure 3-1. Integrated Thin-Film Shifter/Waveguide Combination

Light from the laser is guided into the device by a channel waveguide in the PMMA film. The light is gradually expanded in the horn waveguide region, and then coupled into the guiding layer in the Bragg cell where it interacts with the acoustic wave. After the interaction, the frequency-shifted beam is collected by the second horn and reenters the channel waveguide in the PMMA film which serves as the input channel to the waveguide resonator.

In order to properly design the integrated-frequency shifter and waveguide, it is necessary to: define the frequency shifter material; determine the form and characteristics of the guiding layer in the shifter; calculate the optimum acousto-optic interaction characteristics; define the transducer dimensions corresponding to that interaction; design the most efficient horn waveguide shape; and establish the waveguide matching approach and parameters.

The material selected for the frequency shifter is Lithium Niobate ( $\text{LiNbO}_3$ ), a crystal with excellent electro-optic and acousto-optic properties. Low-loss ( $<1$  dB/cm) optical waveguides are routinely made in the laboratory by diffusing titanium ions into the surface. Efficient surface-acoustic-wave devices have been made in  $\text{LiNbO}_3$  and used in frequency shifting and spectrum analysis devices. Based on the frequency shifting conditions and the optical and acoustic wavelengths used, we have selected an eight-finger transducer design with finger spacing and finger width of four microns, and a transducer length of eight millimeters. The acoustic wavelength for such a device is 13 microns. For efficient operation, the width of the optical beam must be larger than the acoustic wavelength ( $\Lambda$ ) and smaller than the square root of the product of the optical wavelength ( $\lambda_0$ ) and the interaction length ( $l$ ). The optical beam width chosen is 40 microns, midway between the  $\Lambda$  of 13 microns and the  $\sqrt{\lambda_0 l}$  of 70 microns. The parabolic horn shape is chosen in order to adiabatically expand the narrow channel mode (approximately five microns) into the broad interaction mode (40 microns) without exciting other waveguide modes. The horn is 1.6 mm long. The approach to joining the optical waveguide to the  $\text{LiNbO}_3$  waveguide uses butt-end coupling. This technique aligns the vertical centers of the two waveguides and optically contacts them. Light travelling in one waveguide can then be "funnelled" directly into the other, assuming the waveguides are mode matched.

The techniques selected had all been successfully demonstrated in the laboratory. A frequency shifter has been fabricated using the transducer pattern described and operated with 60 percent efficiency at 200 MHz by Northrop. The horn design is based upon a theoretical calculation done at the Naval Research Laboratory.<sup>(6,7)</sup> Devices using this model have been made and have demonstrated high efficiency. The butt-end coupling technique has recently been demonstrated with  $\text{LiNbO}_3$  and plastic waveguides.<sup>(8)</sup> However, the synthesis of these techniques to demonstrate a functioning single-mode waveguide frequency/shifter combination had not yet been accomplished.

### 3.2 DESIGN CONSIDERATIONS

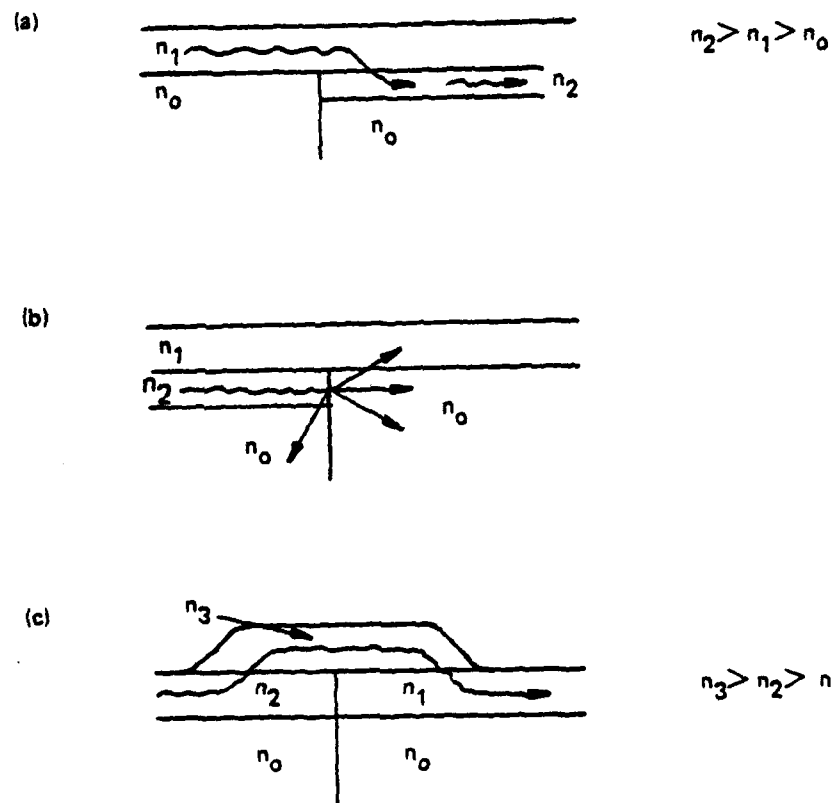
The key aspects of the problem in producing an integrated waveguide/frequency shifter combination are:

1. transferring an optical guided wave from the waveguide into the frequency shifter and back out with minimal disturbance and loss
2. providing a properly shaped, collimated optical beam for efficient acousto-optic interaction
3. collecting only the appropriately shifted beam after the interaction

The difficulty in transferring optical guided waves into and out of the frequency shifter occurs because the index of refraction of the  $\text{LiNbO}_3$  (2.20) is much higher than that of the PMMA waveguides (1.50). Thus, the many waveguide coupling techniques based on evanescent wave-tunnelling cannot be applied reciprocally. For example, tapered coupling can be used to couple light into the  $\text{LiNbO}_3$  chip (see figure 3-2a), since light will characteristically travel in the region of higher refractive index. Once light is travelling in the  $\text{LiNbO}_3$ , however, it will not couple out into the lower index guide (figure 3-2b). Also, there are no suitable materials of higher index that can be used to interconnect the two (figure 3-2c). The tapered end gradually channels the light in  $n_3$  into  $n_1$ . The mismatch in the effective indices of refraction, or equivalently, the mode propagation constant places stringent requirements on any technique to couple light between the guides. The problem is additionally complicated because the spatial distributions of the mode patterns are very dissimilar. In free space, this mode matching is accomplished by suitable lensing and aperturing, techniques not amenable to thin-film implementation. Similar problems occur when matching fibers to waveguides or laser diodes.

In order to provide a proper beam for the acousto-optic interaction, there must be proper control of the mode characteristics, the beam width and the divergence. The optical beam passing through the interaction region must be wide (40 microns for example), collimated (essentially planar over the interaction region of approximately 1 mm), and single mode. The last condition is to ensure a unique effective wavelength and wavevector so as to provide an unambiguous frequency-shifted output.

The collection of the appropriate beam depends mainly on the divergence of the input beam and the angular deflection of the first-order diffracted beam. For the working frequency chosen (200 MHz), the Bragg diffraction is of the order of 1 degree. Thus, the beam divergence must be less than this to provide sufficient resolution after the interaction to extract the desired shifted component. There are two implementations possible: the first in which the light remains laterally confined in a channel waveguide through the interaction in the frequency shifter; and the second in which the waveguide is planar and there is no lateral confinement. It was shown that the horn design parameters are identical, so the simpler, unconfined version was the one chosen.



112H7-3

Figure 3-2. Propagation Between Dissimilar Waveguides



### 3.3 ACOUSTO-OPTIC INTERACTION

The fundamental mechanism for shifting the frequency of the optical signal is an acousto-optic interaction (figure 3-3) which provides a beam deflection and frequency shifter through a Doppler mechanism. A travelling surface acoustic wave is induced in a photoelastic material by a piezoelectric transducer. This strain wave is accompanied by a "refractive index wave" in the material which can be thought of as a refractive index grating travelling through the material at the speed of sound. The incoming light diffracting off the moving grating will be frequency-shifted and deflected. The form of the interaction can be divided into two extreme cases characterized by a dimensionless parameter,  $Q$ :

$$Q = \lambda_{\text{eff}}^2 / \Lambda^2 \sigma n$$

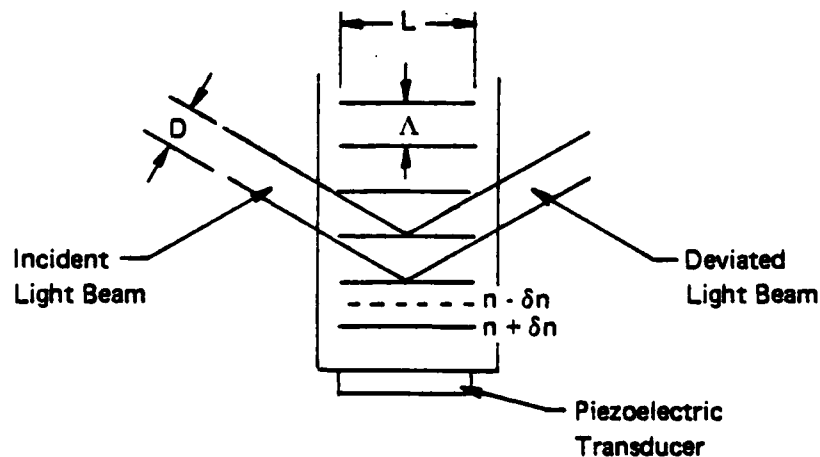
Where  $\lambda_{\text{eff}}$  is the effective wavelength of the light being guided in the material,  $\Lambda$  is the wavelength of sound and  $\sigma n$  is the induced change in index. If  $Q < 1$ , the light beam is split into several beams corresponding to different orders of diffraction and shifted in frequency by integer multiples of the acoustic wavelength. This is referred to as the region of Raman-Nath. If  $Q \gg 1$ , there is only a single diffracted beam shifted in frequency by the acoustic frequency. This is the region of Bragg diffraction and the desired region for frequency shifting; thus, the design criteria are based upon ensuring that  $Q \gg 1$ .

In the Bragg regime, the light is deflected at an angle given by:

$$\sin \theta_B = \lambda_0 / 2n\Lambda$$

The diffracted light is Doppler-shifted and

$$f_{\text{out}} = f_{\text{laser}} \pm f_{\text{sound}}$$



112H7-4

Figure 3-3. Acousto-Optic Interaction

The fraction of laser light deflected is a function of the material and length of interaction, and is given by:

$$I/I_0 = \sin^2 \left[ \frac{\pi l_c}{\sqrt{2\lambda_0}} \sqrt{M I_{\text{acoustic}}} \right]$$

and is therefore maximum when

$$\pi l_c / \sqrt{2\lambda_0} \sqrt{M I_{\text{acoustic}}} = Q/2$$

Here  $l_c$  is the interaction length,  $M$  is a material-dependent constant, and  $I_{\text{acoustic}}$  is the acoustic power.

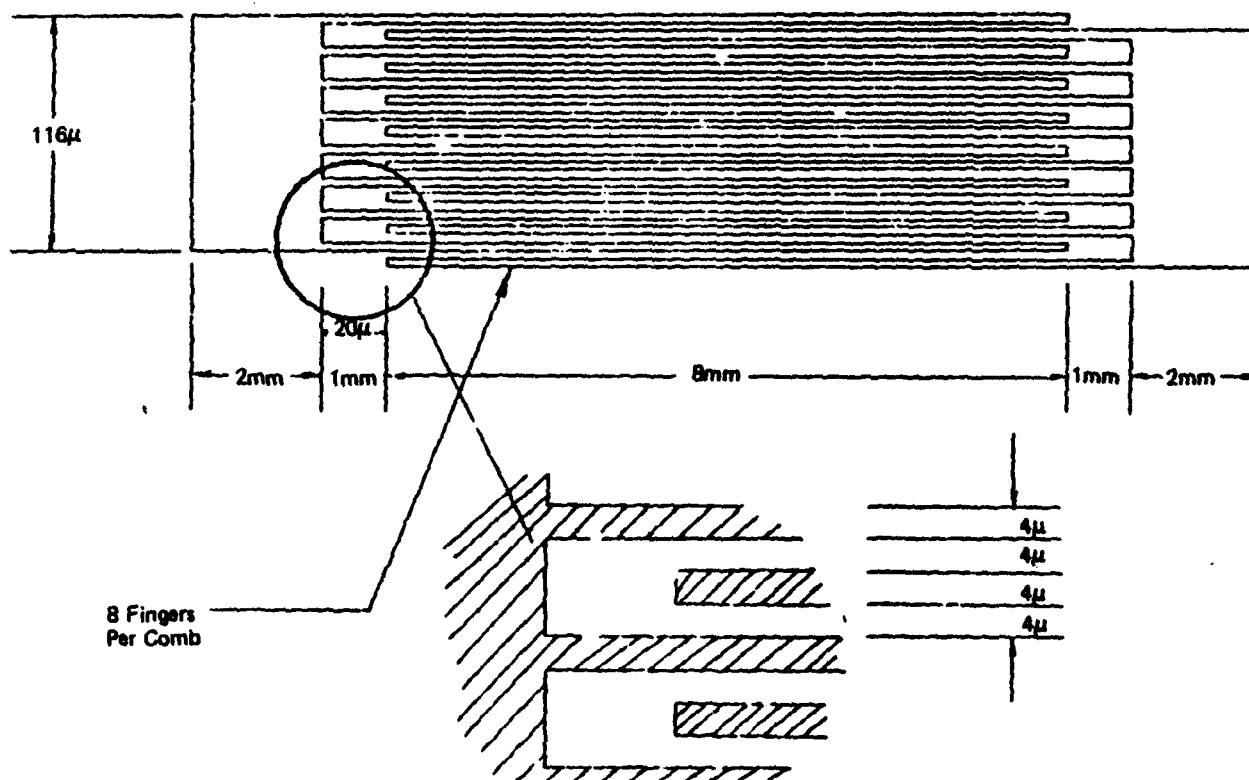
We have used the above formulation to design a frequency shifter on  $\text{LiNbO}_3$ . Assuming  $\lambda_0 = 1\mu\text{m}$ ,  $\theta_B = 1^\circ$ ,  $I_{\text{acoustic}} = 50\text{ mw}$ , and a Y-cut  $\text{LiNbO}_3$  substrate with an X-propagating light wave and z-propagating acoustic wave, we have:

$$\Lambda = 13\mu\text{m}$$

$$f_s = 270\text{ MHz}$$

$$l_c = 3.2\text{ mm}$$

The design of the interdigital transducer (IDT) is shown in figure 3-4.



112N7-6

Figure 3-4. Interdigital Transducer Detail (not to scale)

### 3.4 HORN DESIGN

It is necessary to expand the channel waveguide from its normal width to some larger width in such a way that as much power as possible remains in the lowest mode. Based on considerations of adiabatic propagation in waveguides, this can be done using parabolic horn structures. In the ray model, light propagates down a channel waveguide as shown in figure 3-5a. Here the ray angle  $\theta_j$  for the mode is related to the propagation constant  $\beta_j$  by

$$\beta_j/k = N_g \sin \theta_j$$

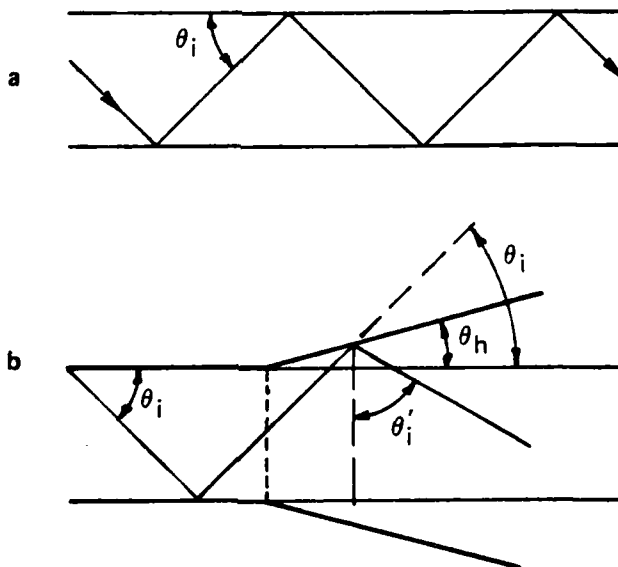
where  $k = 2\pi/\lambda_0$  ( $\lambda_0$  being the free space wavelength), and  $N_g$  is the index of refraction of the waveguide. As the waveguide expands in order to prevent coupling into higher-order modes, the angle of divergence ("horn angle") must be less than the ray angle,  $\theta_j > \theta$  (see figure 3-5b). The mode then propagates smoothly by increasing mode angle  $\theta_j$  corresponding to the equivalent mode in the new waveguide. We can write:

$$\theta_h = \alpha \theta_j (Z)$$

where  $\alpha < 1$  and  $\theta_j (Z)$  is the ray angle of the mode at  $Z$ . As Burns and Milton have shown<sup>(6)</sup>, this approach leads to an optimum shape (for well-confined modes) of a parabola. The width of the horn as a function of length is

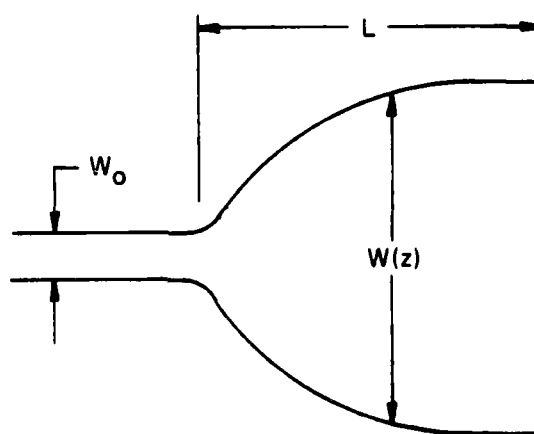
$$W = \sqrt{2 \alpha \lambda_{eff} Z + W_0^2}$$

where  $\alpha$  is a constant  $\geq 1$ ,  $\lambda_{eff}$  is the effective wavelength in the lowest mode of the guide,  $Z$  is distance along the guide, and  $W_0$  is the initial width (see figure 3-6).



112H7-7

Figure 3-5. Ray Propagation in Waveguides



112H7-8

Figure 3-6. Basic Horn Design

### 3.5 DETERMINING WAVEGUIDE HORN WIDTH

The choice of the final width of the horn determines the length and shape of the horn. The final width of the horn must be sufficient to provide efficient interaction in the Bragg regime. This means the maximum width must be large in comparison to the acoustic wavelength. Furthermore, the beam width must remain essentially constant over the interaction region. Since the width  $W$  is determined from the Bragg conditions, we need to find the optimum length and width for the Bragg interaction.

The coupling length given by maximizing the deflection efficiency is 3.2 mm and the transducer fingers are slightly longer (about 3.8 mm), so that the interacting region ( $L$ ) contains planar sound waves. The transit region between the horns (i.e., optical beam input to optical beam collection) is about 5 mm longer.

One condition on the optical beam width ( $W$ ) was that it must exceed the acoustic wavelength

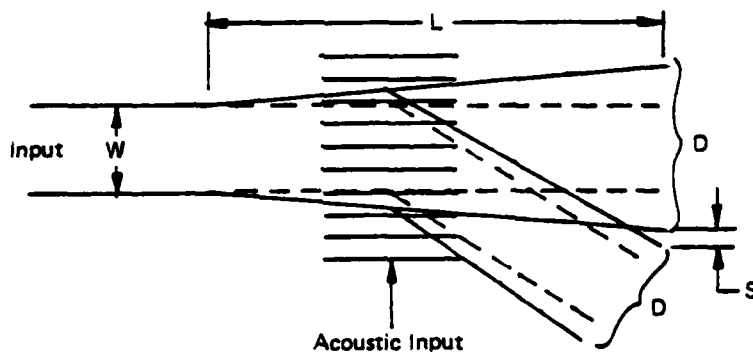
$$W > \Lambda$$

The second condition was determined from resolution requirements of an unconfined beam diverging from the input horn; i.e., the conditions that will ensure that the shifted beam is sufficiently separate from the unshifted.

In terms of the variables defined in figure 3-7, we must choose  $W$  and  $L$  to ensure that  $S$  is sufficiently larger than  $D$ .

That is to say

$$S/D > 1$$



112H7-11

Figure 3-7. Resolution of Diffracted Beam

Now, the separation  $S$  is given in terms of the Bragg angle

$$S = \theta_B L$$

where  $L$  is the interaction length. The beam width  $D$  can be estimated by assuming that the beam has Gaussian propagation characteristic with beam waist  $W$

$$D = W \sqrt{1 + (L/Z_0)^2} \quad Z_0 \equiv W^2/\lambda$$

Thus we require

$$\theta_B (L/W) / \sqrt{1 + (L\lambda/W^2)^2} \geq 1$$

To obtain adequate separation while ensuring that diffraction will not be an important factor, we require simultaneously

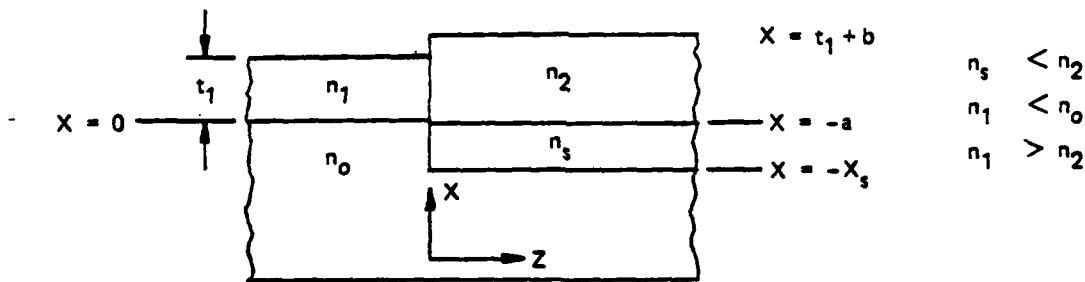
$$L\lambda/W^2 < 1 \text{ and } \theta_B \lambda/W > 1 \quad (\theta_B \approx \Lambda/\lambda); \text{ i.e., } \Lambda/W > 1$$

that is, the width of the beam must be greater than the acoustic wavelength and less than the square root of the product of interaction length and optical wavelength. Thus  $13 \mu\text{m} < W < 200 \mu\text{m}$ .

### 3.5 INTEGRATION APPROACH

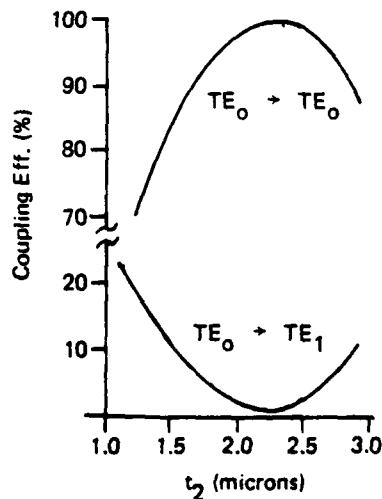
The basic approach relies on "butt-end" coupling; i.e., aligning the two waveguides such that the guiding channel in one lines up exactly with the guiding channel in the other. This exact matching is impossible even in principle because of the dissimilar nature of the two waveguides. We first consider the integration of ideal waveguides, and then the effect of typical fabrication uncertainties. Only the coupling from the LiNbO<sub>3</sub> into the plastic is described in detail.

The ideal junction between the waveguides is shown in figure 3-8. The light will be flowing in the +Z direction in the region of  $n_1$ . This represents the enhanced index of refraction region in the LiNbO<sub>3</sub> ( $n_0$ ) due to the in-diffused titanium. The objective is to efficiently couple this light into the low index waveguide (photolocked into a thin film of PMMA) to the right. The parameters  $b$  and  $a$  must be chosen (given the equivalent waveguide depth  $t_1$  of the LiNbO<sub>3</sub> diffused guide) to maximize power transfer into the plastic. Based on theoretical considerations, optimizing  $t_2 = t_1 + b + a$  for LiNbO<sub>3</sub> polymer waveguides predicts coupling efficiencies of 96 percent for these ideal structures. Furthermore, as shown in figure 3-9, the coupling efficiency is relatively insensitive to  $t_2$ . A variation of  $\pm 0.5$  micron is possible while having coupling efficiency in excess of 90 percent. Note also that coupling into the odd modes (e.g., TE<sub>1</sub>) from the even mode TE<sub>0</sub> is a minimum.



112H7-12

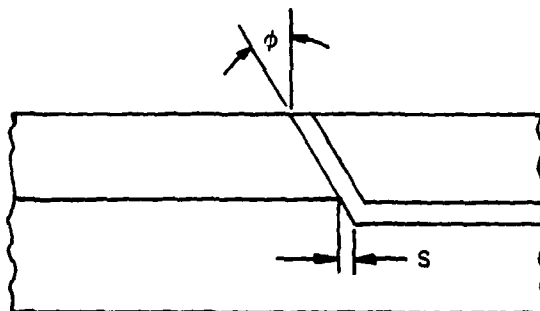
Figure 3-8. Ideal Waveguide Junction



112H7-13

Figure 3-9. Theoretical Coupling Efficiency (LiNbO<sub>3</sub> -> PMMA)

Actual devices will not duplicate the ideal waveguide configuration and will typically appear as shown in figure 3-10. Two parameters derived from waveguide fabrication conditions ( $\phi$ ,  $S$ ) have been examined. These are defined as the angle ( $\phi$ ) of the junction plane with respect to the plane normal to the waveguide axis, and the offset spacing ( $S$ ) between the two guides caused by buffer layer deposition. Calculations show that the tilt can range several degrees while maintaining coupling efficiency to within a few percent. The waveguide spacing,  $S$  can affect coupling since the beam leaving the  $\text{LiNbO}_3$  waveguide will be diffracted before hitting the PMMA waveguide. Significant reduction in coupling will occur for large ( $\sim 15 \mu\text{m}$ ) separations. A third source of coupling loss occurs if the axes of the two waveguides are not collinear. These effects are usually very small for the typical fabrication techniques applicable here. The calculations show that the angle should be kept below  $5^\circ$  and the displacement below  $5 \mu\text{m}$ . This is within the capability of current fabrication techniques, and this method has been demonstrated to produce highly efficient ( $>70$  percent) waveguide couplers. No measurable increase in the angular spread of the incident beam was observed after crossing the junction.



112H7-14

Figure 3-10. Simplified Practical Structure of Junction

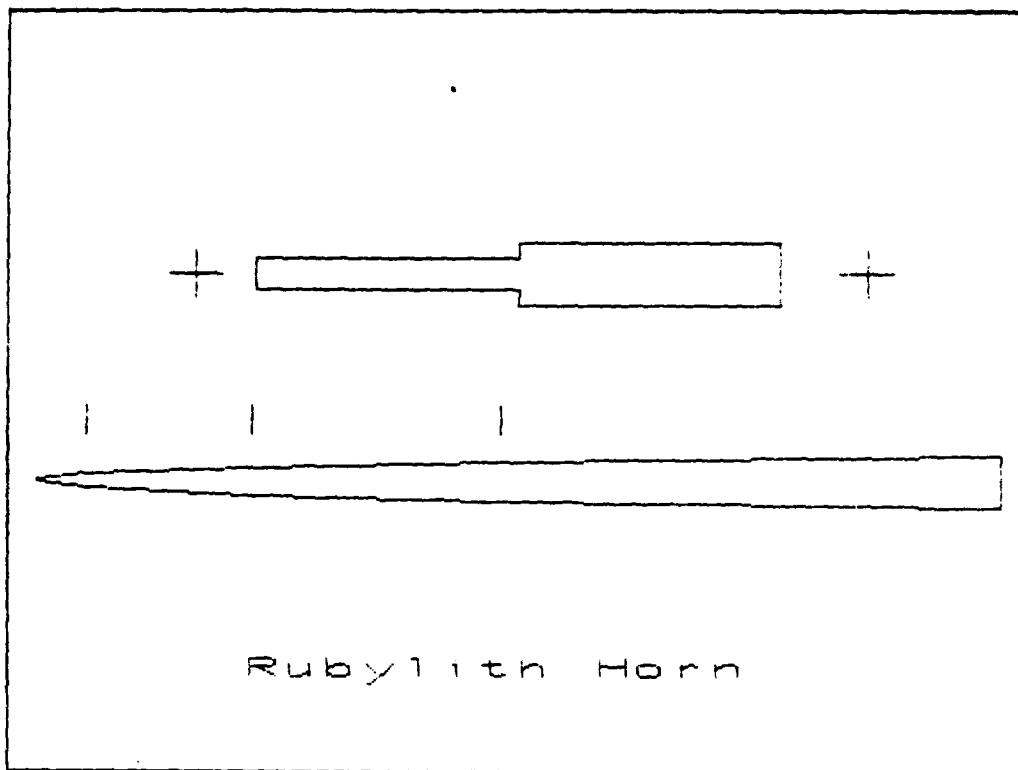


## Section IV

### HORN WAVEGUIDE FABRICATION

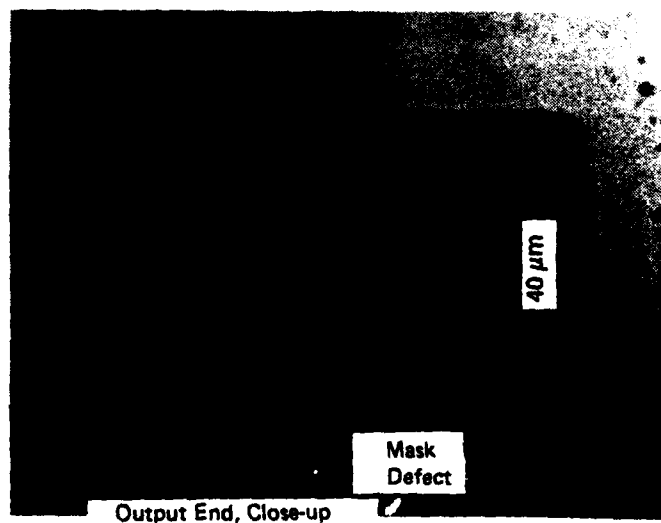
Tapered waveguides and horn waveguides are transitional devices which provide efficient power transfer between bordering waveguide structures having different transverse field distributions. The waveguide frequency shifter must take a narrow, single-mode waveguide input and produce a broad, single-mode beam for the acousto-optic interaction. Where single-mode performance is a requirement, the parabolic horn is preferred. The parabolic horn displays the high throughput and adiabaticity of the simpler tapered waveguide, but can accomplish the desired field expansion or contraction over a shorter length. For z-propagation, the parabolic horn takes the form  $f(z) = Cz^2$  with C a small constant  $\approx 10^{-5}$  for in-diffused waveguides in lithium niobate. While  $f(z)$  as written above is continuous, most fabrication approaches must incorporate some discontinuity in the generated pattern, resulting in what are referred to as segmented parabolas.

The first attempt at parabolic horn fabrication used a fairly traditional approach once used in the production of simple printed circuit boards: the photoreduction of a design cut in rubylith to final size on a precision glass photomask. The design for the segmented parabolic horn was decided upon early in 1982 and a drawing made which was translated to a rubylith sheet by PPD (see figure 4-1). The horn, in its final configuration, was composed of four segments which would gently transform the transverse field width between turning points from 5 microns to 40 microns over a distance of approximately 5.5 millimeters. To enable the realization of accurate artwork while remaining within bounds defined by available equipment, the rubylith horn was cut 165 times actual size at nearly at meter's length. An outside vendor performed the reduction and supplied the pattern with alignment masks on a 4 x 4 inch iron-oxide photomask. Microscopic inspection of the mask (see figure 4-2) showed that while adherence to design specification was good, flaws in the original rubylith artwork were fairly conspicuous on the mask and were of wavelength size. It was believed that although these flaws would increase losses and intermode scattering in the final in-diffused waveguide, those losses would be fairly small due to the slight pattern washout accompanying the diffusion process. This particular photomask was used to establish certain photolithographic process parameters independent of the chlorobenzene hardening step. In addition, an attempt to expose the photolocking PMMA solution normally used in resonator fabrication was done with this particular mask and a 1000 W HeXe illuminator. It was believed that while the horn was not optimized for PMMA, the experiment would establish the feasibility of the method for passive device fabrication. The PMMA used for resonator fabrication was not sufficiently photosensitive to yield a parabolic guiding structure and this approach was discontinued pending modifications of the polymer formulation.



21227-16

**Figure 4-1. Schematic of Rubylith Artwork.** Original was nearly one meter long to enable accurate scaling. Line segments above horn illustrate position of discontinuities of parabolic approximation.



21227-17

**Figure 4-2. Microphotograph of Rubylith Horn Pattern in Photoresist.** Dust particles in microscope objective, not the resist.

Later in 1982 an experiment was performed to investigate the possibility of horn fabrication by direct laser writing in PMMA. In this experiment, a quartz disk was coated with a thin ( $\approx 3 \mu\text{m}$ ) layer of PMMA as if for use in resonator fabrication. This coated disk was then fixed in the laser writing apparatus such that the disk's normal was at a large angle ( $\approx 17.5^\circ$ ) with respect to the axis of the focused UV beam. As the beam passed over the disk in the plane defined by the disk normal and the beam axis, the PMMA was exposed such that the resulting waveguide could be very well described as a product of gaussian exponentials. Optical testing of this structure revealed that while the guide was highly multimode, it displayed some mode-preserving qualities very near the guide waist. Calculation of induced index change as a function of position along the guide showed that the index increased nearly linearly as proximity to the guide waist increased; thus in this region it may be said that the structure performed as would a simple taper. Later comparison of the dimensional properties of the laser-written horn with computed laser-deposited energy density (see figures 4-3 and 4-4) has raised some questions regarding the nature of the photolocking process and the effects of dopant mobility and, perhaps, crosslinking. Given adequate control of film performance, it seems that direct laser writing of horns in PMMA is indeed feasible.

Photosensitive dopant mobility is near zero in baked-out photoresists; therefore, given some control over the height of the focal point above a resist-coated substrate, parabolic horns of essentially perfect continuity may be laser written to specification. Computer control of disk position with respect to the beam focal point, disk speed and/or UV intensity would allow the fabrication of horn/resonator photomasks which could be used in conjunction with the SAW frequency shifter masks. Details of the experiments for a horn waveguide fabricated by this technique are given in Appendix A.

Commercial pattern generation of very high resolution is performed by computerized mechanism. In pattern generation, a size-programmable rectangular aperture is fixed very near a precisely movable translation/rotation stage which holds a coated glass plate intended to become a photomask. The stage moves as the aperture opens and closes according to a program agreed upon by designer and vendor. Usually the resulting mask is a compromise between the ideal and cost.

The mask designed by PPD and produced by pattern generation outside PPD incorporated two segmented parabolic horns which were connected at their wide ends by a trapezoidal interaction region and were noncoaxial by  $1^\circ$ . The horns were identical to the Rubylith/photoreduction horn except for the addition of short ( $5 \mu\text{m}$ ) waveguides at their narrow ends. The interaction region was approximately 8.5 mm long by 300  $\mu\text{m}$  wide. Careful attention was paid to the quality of the horn edges so that losses due to scattering in the final waveguides would be only minimally related to mask defects. In making a frequency shifter, this mask would be utilized after a 5  $\mu\text{m}$  wide channel was cut in a resist-coated Lithium Niobate substrate. Subsequent in-diffusion of Titanium and placement of SAW IDTs would result in a "full-shifter." The mask was fabricated (figure 4-5) but has not been evaluated.

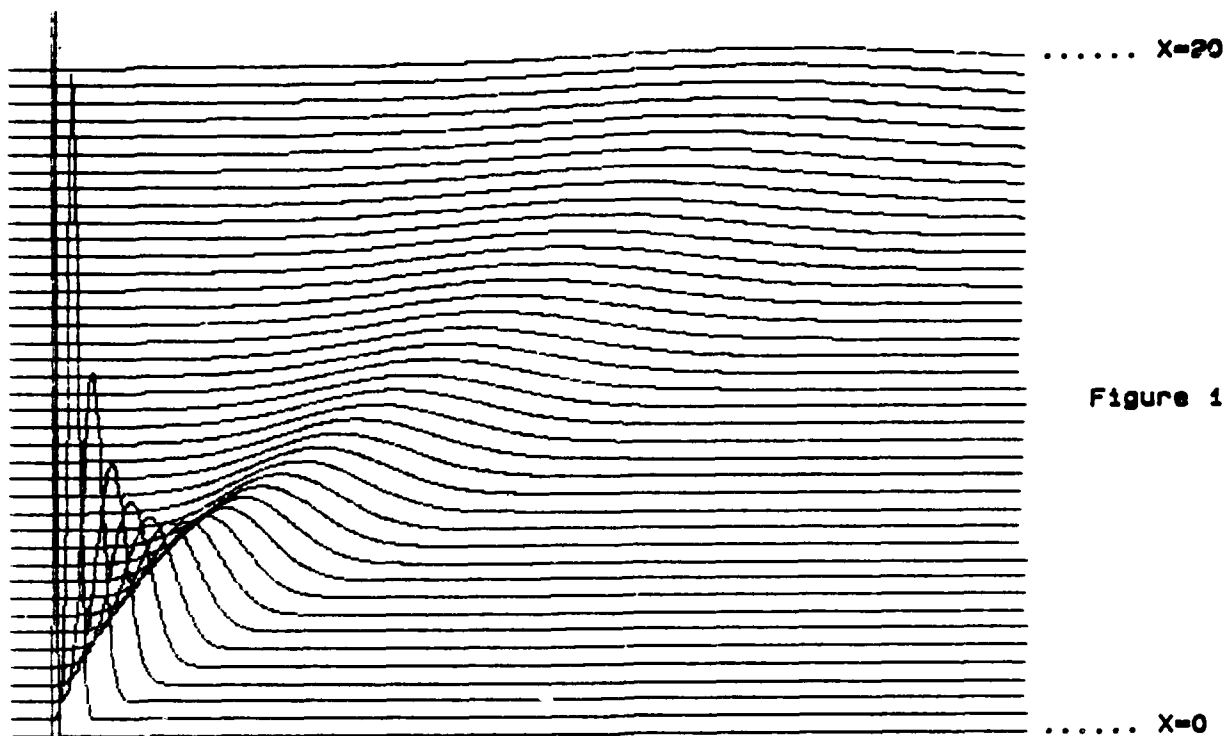


Figure 1

21227-14

Figure 4-3. Calculated Laser-Written Energy Density for PMMA Horn. Z  
Peak at  $X = 0$  is approximately 100 times that at  $X = 5$ .

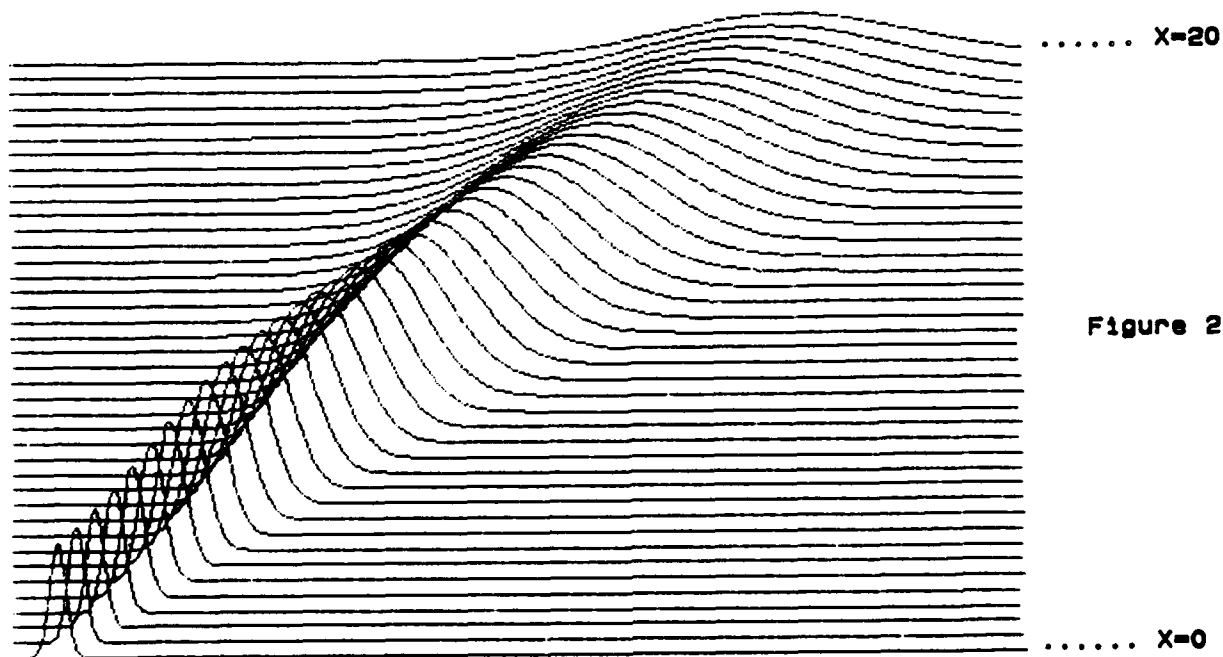


Figure 2

21227-15

Figure 4-4. Resultant Dimensional Change in PMMA Film. Note the evidence of saturation near  $X = 0$ . Peak at  $X = 0$  is about 1400 Angstroms. LWHM is 18 microns.

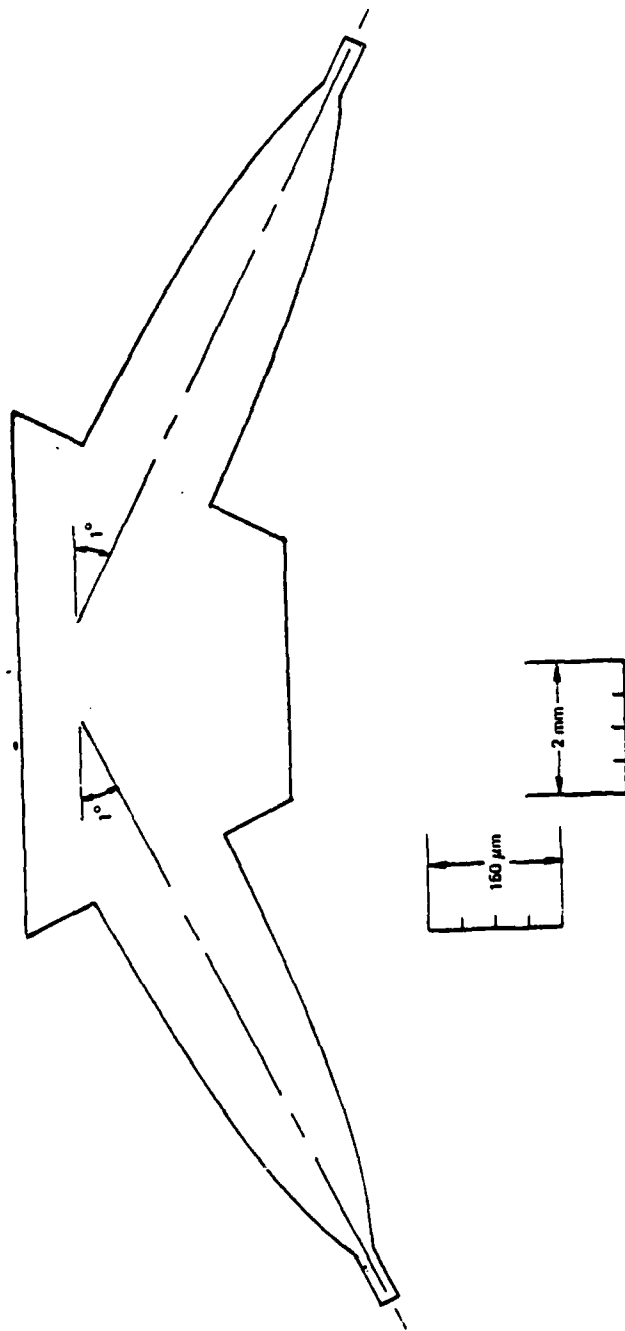


Figure 4-5. Full Frequency Shifter Horn Design

21221-20

## Section V

### LiNbO<sub>3</sub>-POLYMER COUPLING

The technology experiments for lithium niobate-polymer waveguide coupling provide the basis for integrating the lithium niobate frequency shifters with the polymer waveguide resonators. The approach chosen was a combination of a step etch based approach which had achieved extremely high efficiencies in laboratory experiments, and a flip-chip approach used for lithium niobate-fiber coupling. The steps involved are:

- In-diffused titanium waveguide in lithium niobate
- Etch step(s) in lithium niobate
- Coat buffer layer on step
- Coat waveguide on step
- Mount lithium niobate on quartz
- Coat waveguide film

Experiments in this area were hampered by the inability to properly etch a step in the lithium niobate. The fabrication of titanium in-diffused waveguides is identical to the procedure used in frequency shifter fabrication and has been described in section IV. In this section, the attempts to step etch are described, along with the integration experiments attempted without the step-etched crystal.

It was determined that for the thickness of the waveguide in the lithium niobate, a step height of 6 to 8 microns would be required. The edge quality (as determined by the smoothness of the step wall, the angle of the step wall with the plane of the waveguide, and the straightness of the edge) is critical to the coupler efficiency. Ion milling would seem the most suitable method for generating this type of step; however, this equipment will not be in place at PPD until 1983. Work to date has used cylindrical and planar RRF (13.56 MHz) sputtering systems.

Conventional sputter masks would not satisfy the requirements for step edge quality. The mask selected was a cleaved edge gallium arsenide crystal. In order to avoid edge rounding, the mask thickness (T) must be

$$T \gg [(E_s t)/E_M]$$

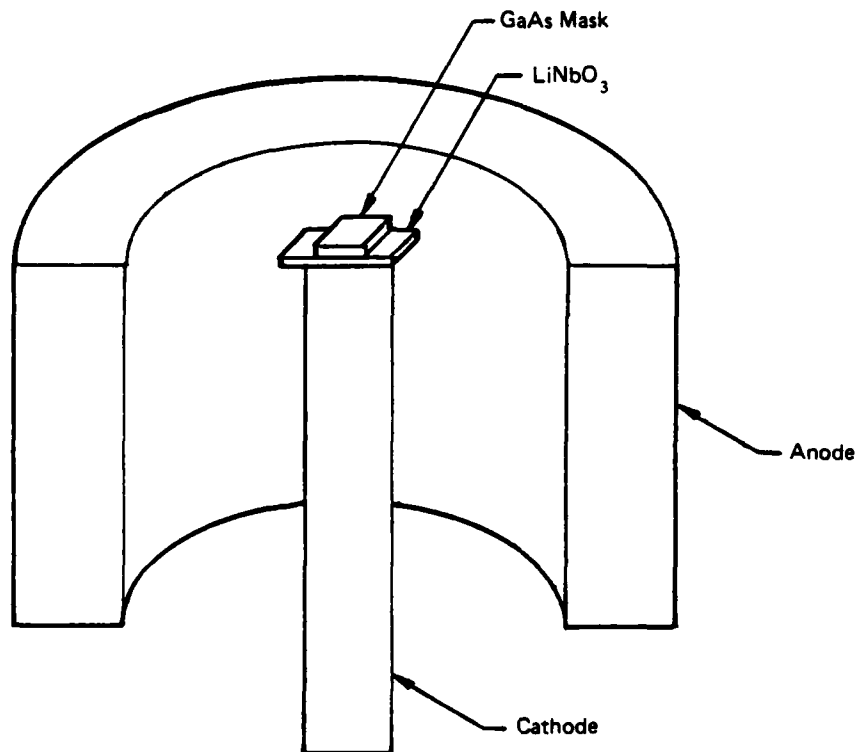
where

- $E_s$  = etch rate of crystal
- $t$  = desired step depth
- $E_M$  = etch rate of maskant

In the case in question, the expression is valued at  $3.2 \mu$ , and a minimum mask thickness of  $500 \mu$  was set. Crystals with a thickness of  $\sim 750 \mu$  were found to cleave reasonably well and still meet the minimum thickness.

Step etching was first attempted using a cylindrical plasma system (see figure 5-1). While the step depth was reached in a reasonably short time, back sputtering of the gallium arsenide mask onto the vertical and horizontal surfaces made evaluation of the step impossible. An attempt to chemically remove the maskant debris from the step resulted in severe damage to the lithium niobate waveguide. A further attempt to operate the system at lower argon pressures and low power inputs (in order to reduce back sputtering) failed due to system instabilities at the lowered operating parameters.

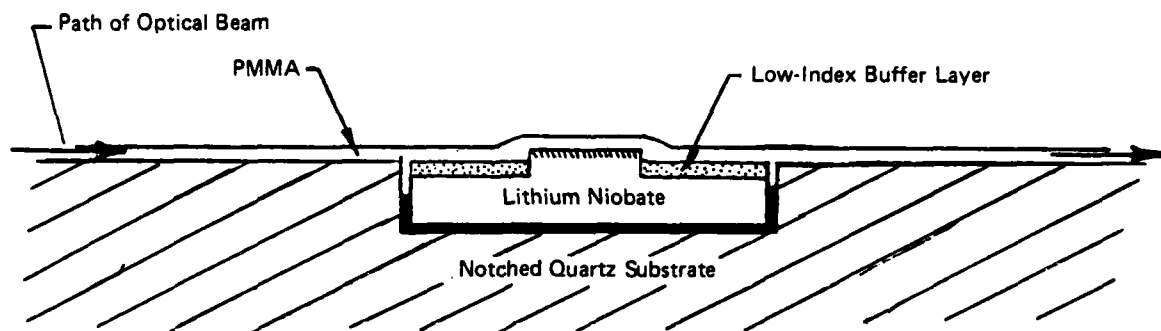
Production loading on in-house sputtering systems required that we use external facilities for planar sputtering experiments. A contract was let to the Millis Corporation in mid-1982. Samples and masks were provided and several attempts were made to produce step edge crystals. Etch rates were found to be several orders of magnitude less than indicated in the literature. It is felt that either the paper is substantially in error in the calculation of power density, or that there is a substantial difference in measurement technique between the two parties.



21227-1

Figure 5-1. Cylindrical Plasma System

One integration scheme involved the placement of the frequency shifter into a precision ground notched quartz substrate. Once the shifter was suitably fixed, given a close enough fit, a PMMA film could be spun over the assembly, effectively joining the materials optically (see figure 5-2). Dimensional tolerances of less than a micron were necessary for achieving satisfactory coupling efficiency. Practical questions included the stability and reproducibility of the quartz/LN bond and the coverage of dimensional gaps by PMMA.



21227-2

Figure 5-2. Frequency Shifter in Notched Quartz Substrate

To test bonding and polymer coverage, an experiment was performed where a "cleaved" fused quartz microscope slide was attached with optical cement on a large fused quartz substrate and rejoined. The substrate was polished to a commercial 80/50 (scratch/dig) and was flat to approximately  $\lambda/2$ . The slide was flame polished by the manufacturer and had the same flatness. All components were cleaned before assembly in a semi-clean environment. The cement used was a medium-to-low-viscosity ( $\sim 400$  cst) epoxy, highly transmissive in the visible and having low expansion during cure. Care was taken to join the slide halves as closely as possible by performing the assembly under microscope. The assembly was clamped using another flat quartz substrate to help achieve coplanarity of the top surfaces of the slides. The curing was done in air at room temperature for two days. Care was taken to avoid the formation of an epoxy bead at the junction of the slides.

After cure and before overcoating with PMMA, the assembly was inspected using a Zeiss interferometric microscope and a Dektak profilometer. It was found that, probably due to epoxy creep during cure, the slide halves had drifted apart approximately 8 microns and were not coplanar. The height difference traced by the profilometer at one location of the junction was 15 microns. Since PMMA film thickness as fabricated was 3 to 4 microns, it was known that unless the polymer filled the gap between slide halves, light guidance across the gap would be very small. Examination of the gap region after coating of the assembly with PMMA revealed that the polymer had not filled the gap, resulting in a discontinuity across the slides. Inspection using a Zeiss also revealed gross nonuniformity in the film thickness and general decrease in quality in the immediate vicinity of the junction. A large amount of scattering was observed there when guided modes were excited in the waveguides. While this technique may eventually be appropriate, these experiments demonstrated that precise and time-consuming grinding and polishing to exacting tolerances as well as extensive experimentation with adhesives would be necessary.

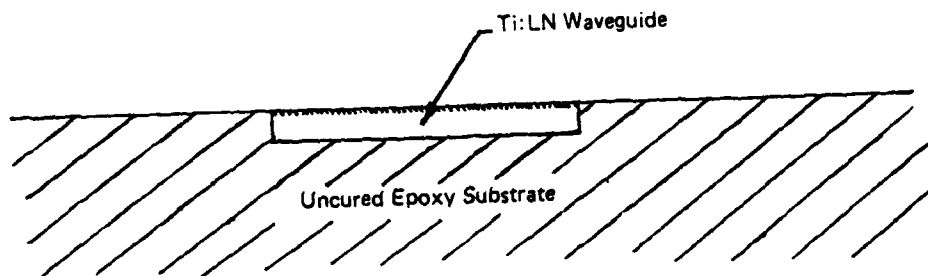


Another approach was attempted which incorporated the casting of a frequency shifter in epoxy (figure 5-3). Given that the plane of the epoxy surface and the plane of the shifter surface were coincident at the outset of curing, the predictable shrinkage of epoxy during cure would yield a small step which could be utilized for end-fire coupling from a polymer guiding layer later spun onto the epoxy substrate. If successful, this method would reduce the integration problem from one of strict dimensional control to strict process control.

The mold consisted of a tightly stretched 50 micron thick mylar film in a steel frame. The frame was such that it could be disassembled after epoxy hardening to release the film and the molded substrate. A Ti:LN waveguide was overturned and weighted in contact with the mylar film (figure 5-4). After pouring the epoxy, the mold was placed in a moderate vacuum (about  $10^{-3}$  mm Hg) and the epoxy was allowed to cure for two days. After release from the mold and before spin coating with PMMA, the assembly was examined using the Dektac profilometer.

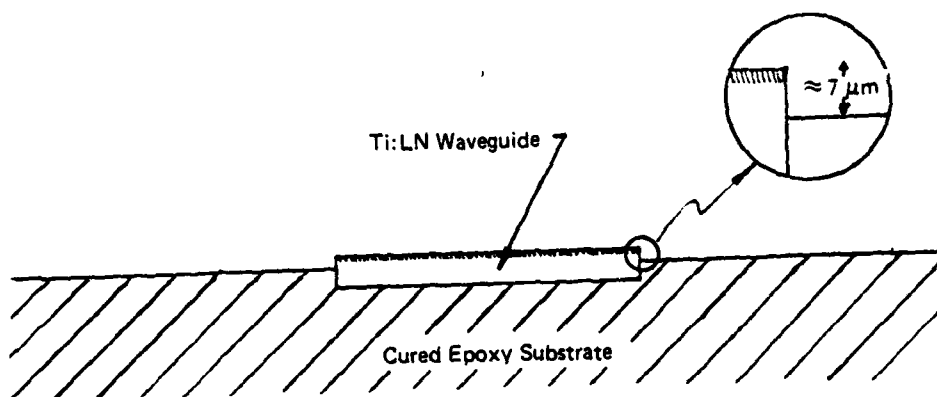
Profilometer examination showed that there was essentially no gap between the Ti:LN waveguide and the epoxy at the surface. However, where a recession of epoxy from the surface of the waveguide was expected, none was found. Instead the epoxy had remained in the form of a taper of decreasing width as it approached the Ti:LN surface (see figure 5-5).

This taper obscured the Ti:LN waveguide and hence precluded the end-fire coupling of light from the side. Other problems were encountered regarding epoxy surface roughness and surface discontinuity at the LN/epoxy interface, which rendered the application of high-quality PMMA films difficult. While this method avoids the difficult dimensional tolerances inherent in the previous method, it requires a careful evaluation of many different casting epoxies with regard to porosity, cure shrinkage, refractive index, absorption, and wetting characteristics.



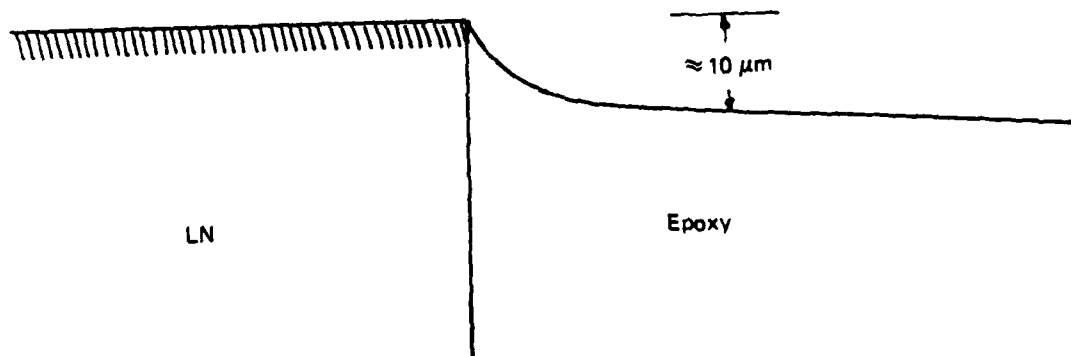
21227-3

Figure 5-3. First Stage of the Ideal Casting of Ti:LN in Epoxy



21227-4

Figure 5-4. After Cure - Ideal



21227-5

Figure 5-5. After Cure - Real

## Section VI

### SAW DEVICE FABRICATION

The first step in fabricating planar frequency shifters is to create the optical waveguide. The waveguides used by Northrop for this contract were made by diffusing titanium into the surface of a lithium niobate crystal. The titanium ions in the  $\text{LiNbO}_3$  lattice raise the index of refraction. Both the ordinary ( $n_o$ ) and extraordinary ( $n_e$ ) indices are raised. The technique provides easily controlled waveguides of the desired mode characteristics which are generally of good optical quality, typically with losses of 1 dB/cm or less.

At PPD the polished surface of the substrate, acoustic grade y-cut  $\text{LiNbO}_3$ , is inspected and the crystal carefully cleaned. A thin layer of titanium is sputter deposited on the surface. The crystal is then heated in a quartz diffusion furnace at  $1000^\circ\text{C}$  to diffuse the titanium into the crystal. The amount of index change and depth of diffusion is determined primarily by the diffusion temperature. The original titanium film thickness also influences the diffusion profile.

Generation of SAWs of such high frequencies is enabled by transducers, or interdigital transducers (IDTs) whose features are of micron or submicron dimension. These dimensions are commonplace in the microelectronics industry, and are attained by the process known as photolithography. In that process, the waveguide/substrate is first coated with a radiation-sensitive polymer film, photoresist. The coated guide is then exposed to ultraviolet radiation passing through an IDT pattern delineated on a photomask. Immersion of the patterned waveguide in photographic developer solution then removes the unwanted photoresist, leaving the IDT pattern on the waveguide. Metal deposition and subsequent removal of the remaining photoresist using a solvent completes the fabrication process of metal IDTs on the waveguide.

In January 1982 representatives of PPD were sent to NRTC to initiate the transfer of photolithographic technology to PPD. At NRTC where the process was quite well known, a technician walked through the process with a PPD engineer, defining the step sequence, some necessary hardware, and some fabrication parameters associated with photoresist obtainable from Kodak. Although the walkthrough did not result in a working frequency shifter, the effort did illustrate some of the flaws which could arise from the fabrication procedure due to its inherent complexity. Photomasks of NRTC design were obtained for use at PPD in process start-up and for fabrication of PPD's first frequency shifters.

Initially, and until late in 1982, PPD facilities associated with photolithography were for the most part borrowed from or shared with those associated with polymer waveguide work. The shared facilities included use of the Class 100 waveguide fabrication room, its wafer coating machine, its convection oven and laminar flow hood. To avoid contamination of the very-low-loss PMMA (used in waveguide work) by the high-loss photoresist, strict scheduling was maintained so that no photolithography was performed while waveguide work proceeded and vice versa. Changeover from one process to the other was always punctuated with a thorough clean-up and segregation of glassware and tools. A special vapor hood was built and installed over the wafer coating machine and separate sloughing skirts obtained. The new solar illuminator, to be described later, gave rise to room temperature control problems due to its multikilowatt heat

dissipation. The cross-contamination, venting and temperature problems limited the capability of photolithography and resonator fabrication. It was apparent that a separate facility had to be constructed. A facility was designed in the fall of 1982 and construction began in December. The room, shown in figure 6-1, will be a safe-lit Class 10,000 clean room, temperature controlled to  $21 \pm 1^\circ\text{C}$ , and humidity controlled to  $40 \pm 3$  percent RH. The photolithography room will be outfitted with an explosion-proof fume hood for liquid filtration and for substrate preparation with certain aromatic solvents and reagents. Clean work will be made possible by the presence of a filtering laminar flow station, also safelited and outfitted with an ozone-free 1000 W Hg-Xe solar illuminator, vacuum-chuck alignment fixture, and precision wafer coating machine. Photoresist bakeout will be performed in a wall-mounted ventable convection oven, development in a temperature controlled bath accurate to  $\pm 0.5^\circ\text{C}$ , rinse-off in a chemist's sink. Midstream and final inspection will be performed using a special phase-contrast microscope. Photoresist life will be extended by storage in a small explosionproof refrigerator. This room, will be complete in January 1983.

The photolithography steps involved in the fabrication process of a PPD frequency shifter are: surface preparation, spin coating, exposure, development, deposition, and liftoff.

Proper photoresist adhesion requires absolute cleanliness of the surface of the substrate to which the photoresist is applied. It was determined that, after the surface preparation employed in waveguide in-diffusion, it is sufficient to use a high-velocity warm acetone spray followed by a filtered ( $0.2 \mu\text{m}$ ) isopropyl alcohol rinse and filtered ( $0.5 \mu\text{m}$ ) dry nitrogen blow-dry. The warm acetone dissolves nearly all inorganics left on the waveguide, the high-velocity spray serves to knock loose any of the larger dust or other particles which may have fallen on the waveguide after its fabrication. The alcohol soak serves to remove the water which condenses on the waveguide during the spray, as well as to disperse any static charge left on the substrate. We have achieved streak-free, pinhole-free coatings of photoresist on lithium niobate to date using this procedure.

Once cleaned, the waveguide is mounted on the vacuum chuck of a high-acceleration wafer coating machine (figure 6-2). Filtered ( $0.2 \mu\text{m}$ ) AZ-1370 positive photoresist is statically dispensed and the waveguide is spin-accelerated at 10,000 RPM/second to 3000 RPM for 20 seconds. Under these conditions, the manufacturer's predicted good film surface quality and film thickness of  $1.3 \mu\text{m}$  have been verified at PPD by profilometer measurement.

After baking the coated waveguide at  $90^\circ\text{C}$  for 20 minutes in an air convection oven, it and a clean IDT patterned photomask are blown off with filtered dry nitrogen and mounted in their proper places on the illuminator's alignment fixture (figure 6-3). After any necessary alignment, the photomask is brought into vacuum contact with the coated waveguide. This kind of special care must be taken in order to avoid or minimize the diffraction-related pattern defects arising from wavelength size dust particles and pattern linewidths. Line broadening of the intended pattern can also result if exposure times are excessive since the diffraction effect of sharply defined boundaries in the mask, while minimized, still exists. Since photoresist may be considered exposed if energy incident upon it exceeds an inherent threshold energy density (defined by the photoresist chemistry), overexposure can lead to the diffracted energy density's exceeding that threshold and to subsequent line broadening or wash-out. It has been empirically found that exposure times of 40 to 60 seconds for this film, depending upon substrate reflectivity, are sufficient for consistent pattern definition with minimum wash-out.

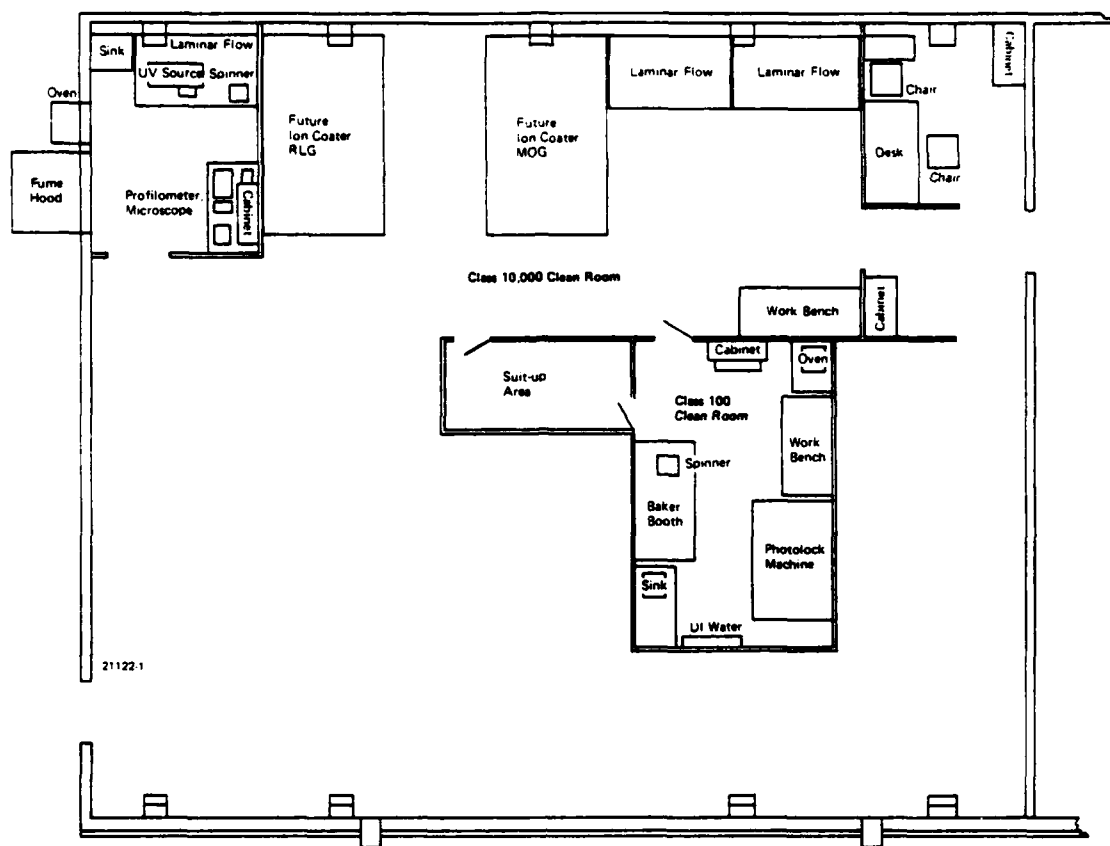
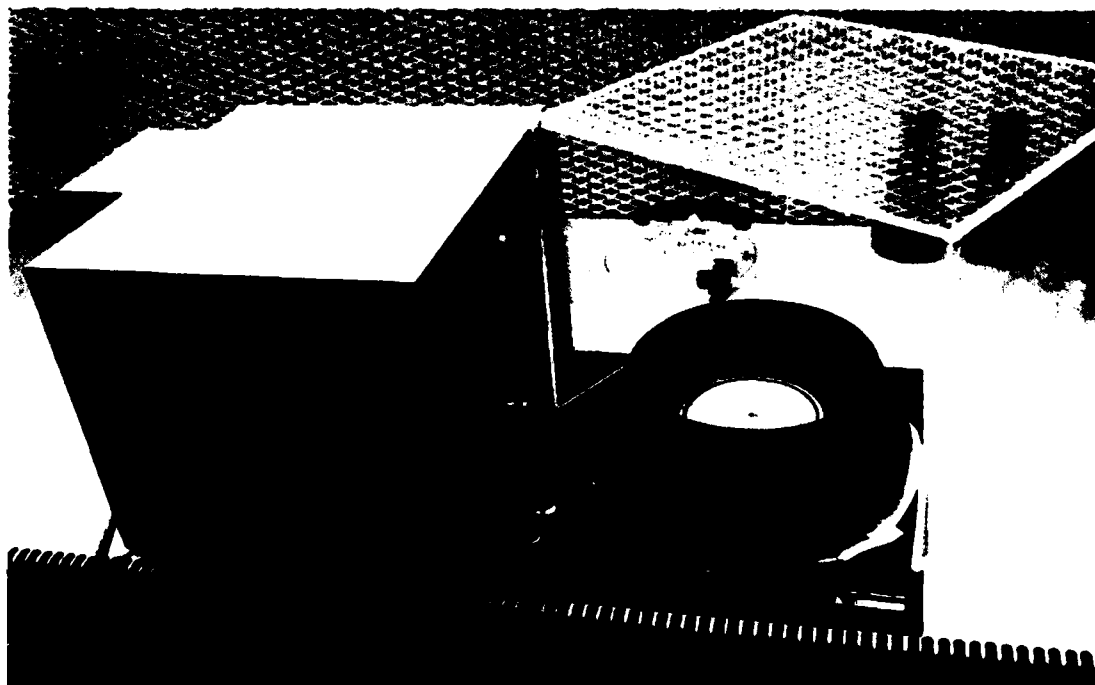
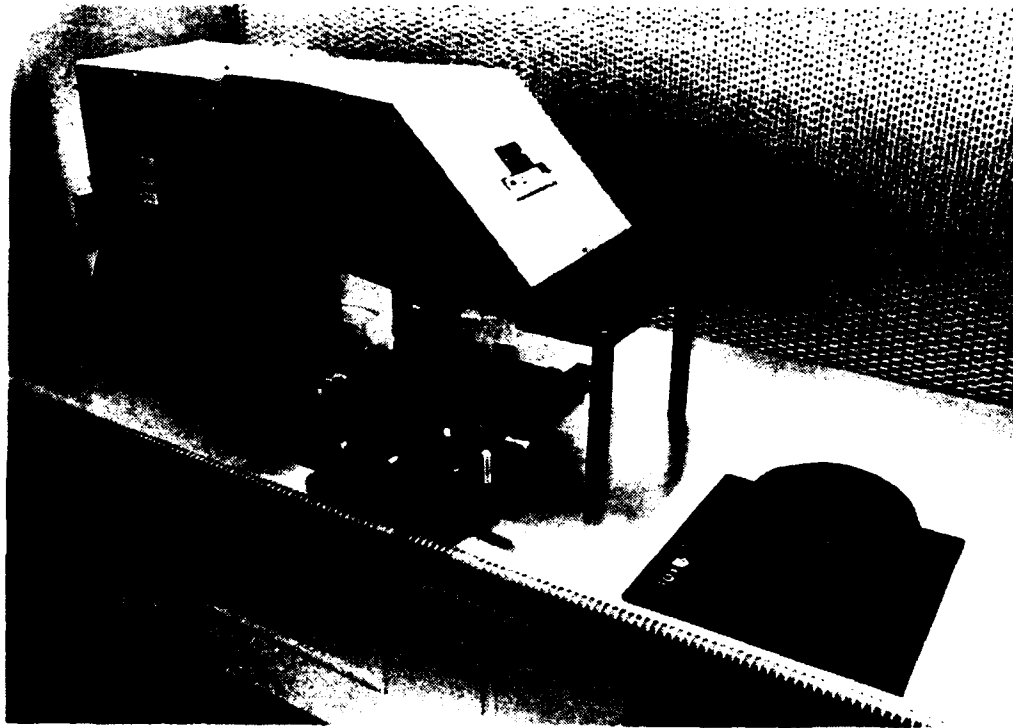


Figure 6-1. Photolithography Area



N908C-1  
01G22-21

Figure 6-2. Wafer Coating Machine



21122-5

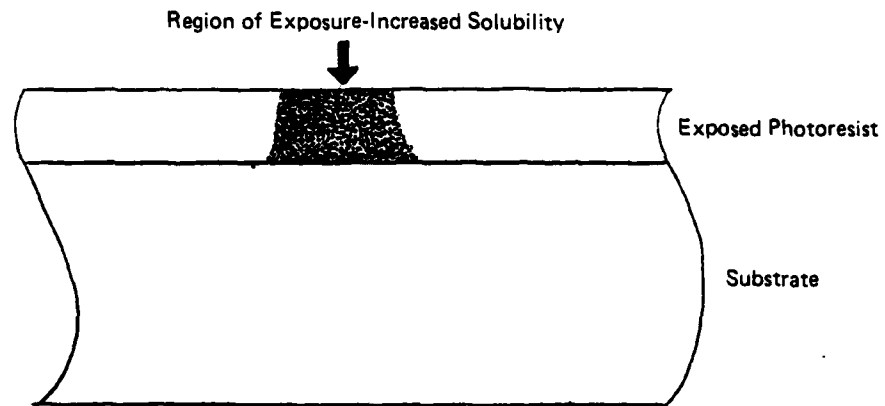
**Figure 6-3. Alignment Fixture**

The metallization of patterns on substrates is more reliably realized if special care is taken to form undercut photoresist profiles. This undercutting leads to a shadowing effect during metal deposition and serves to break the continuity of the metal coating in the well-defined vicinity of the pattern boundary.

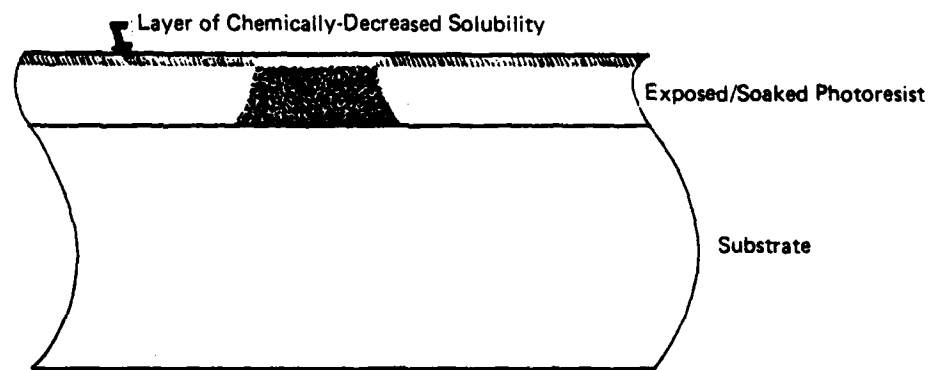
The soaking of AZ photoresist coated substrates in an aromatic solvent such as chlorobenzene lowers the photoresist solubility at and below the surface during development. Strict control of soak time implies equally strict control of the depth of the decreased-solubility layer for strength and undercut. The steps in this process are shown in figure 6-4. Our analysis of published SEM micrographs of chlorobenzene-induced lip photoresist structures and a comparison with known photoresist parameters allowed us to generate similar photoresist profiles. Verification of the lip's existence in the absence of a SEM was enabled by inference after studying photoresist pattern performance and varying development parameters. Lip thickness of 800 to 1000 Å with an undercut of 4000 to 6000 Å has been induced by soaking the resist-coated waveguide for 12 minutes in filtered (0.5 µm) chlorobenzene held at  $21 \pm 2^\circ\text{C}$ , blow-drying with filtered dry nitrogen, baking in an air convection oven for 20 minutes at  $90^\circ\text{C}$ , and developing in a 3:1 AZ-351 to deionized water mixture for 77 seconds at  $21 \pm 0.5^\circ\text{C}$ . A sketch of a typical lip is shown in figure 6-5.

Phase-contrast microscope inspection of the patterned photoresist enables the technician to decide whether the procedure yielded a geometry worthy of metal deposition giving subsequent liftoff success. Some of the flaws possible which may preclude successful liftoff are diffraction related and have been previously mentioned; others include photoresist adhesion failure, collapsed chlorobenzene lip, pattern granularity, scumming, inadequate lip undercut, and general uncleanliness. Figure 6-6 shows a collapsed lip (tableclothing) and a photomicrograph of the resulting pattern.

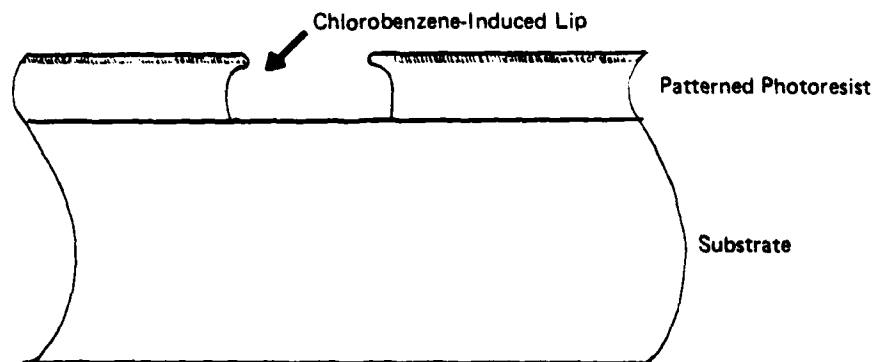
**A) Exposure**



**B) Chlorobenzene Soak/Bake-out**

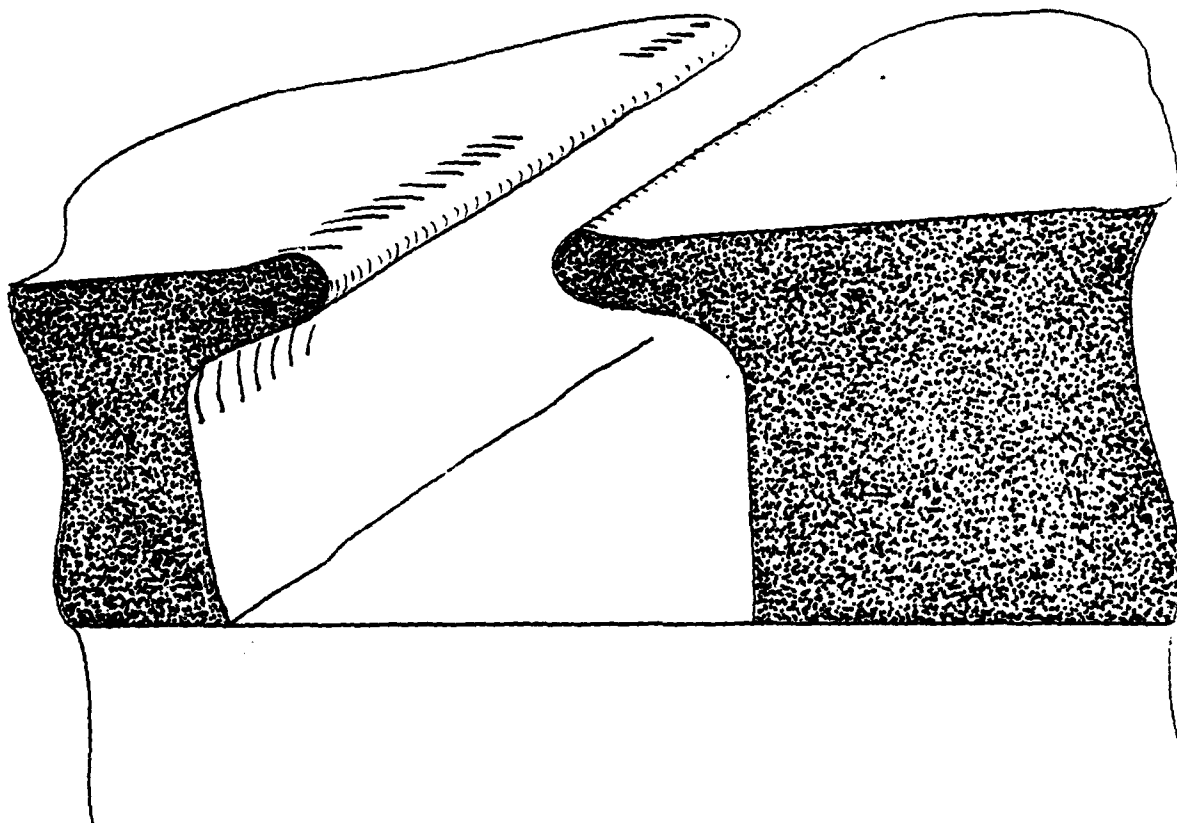


**C) Development**



21227-6

**Figure 6-4. Chlorobenzene-Induced Lip Process**



21227-11

Figure 6-5. Chlorobenzene-Induced Lip in AZ-1370 Photoresist

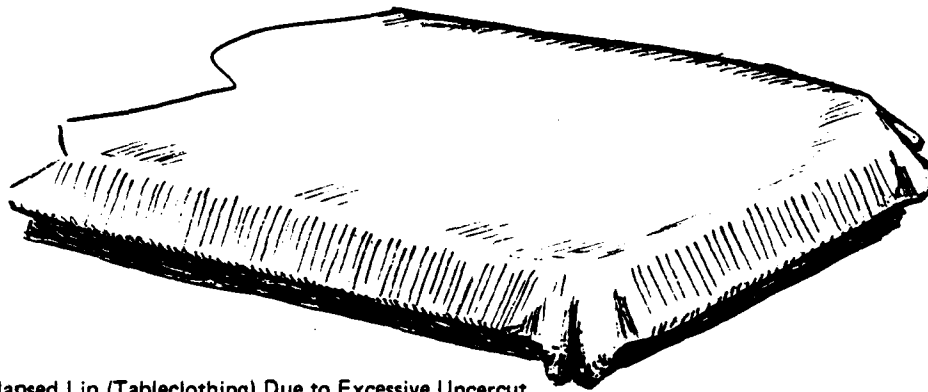




500 X

'Tablecloth' type collapse  
of chlorobenzene lip.

Note general poor line quality  
due to diffraction of UV  
around particles on photo  
mask.



Collapsed Lip (Tableclothing) Due to Excessive Uncerut

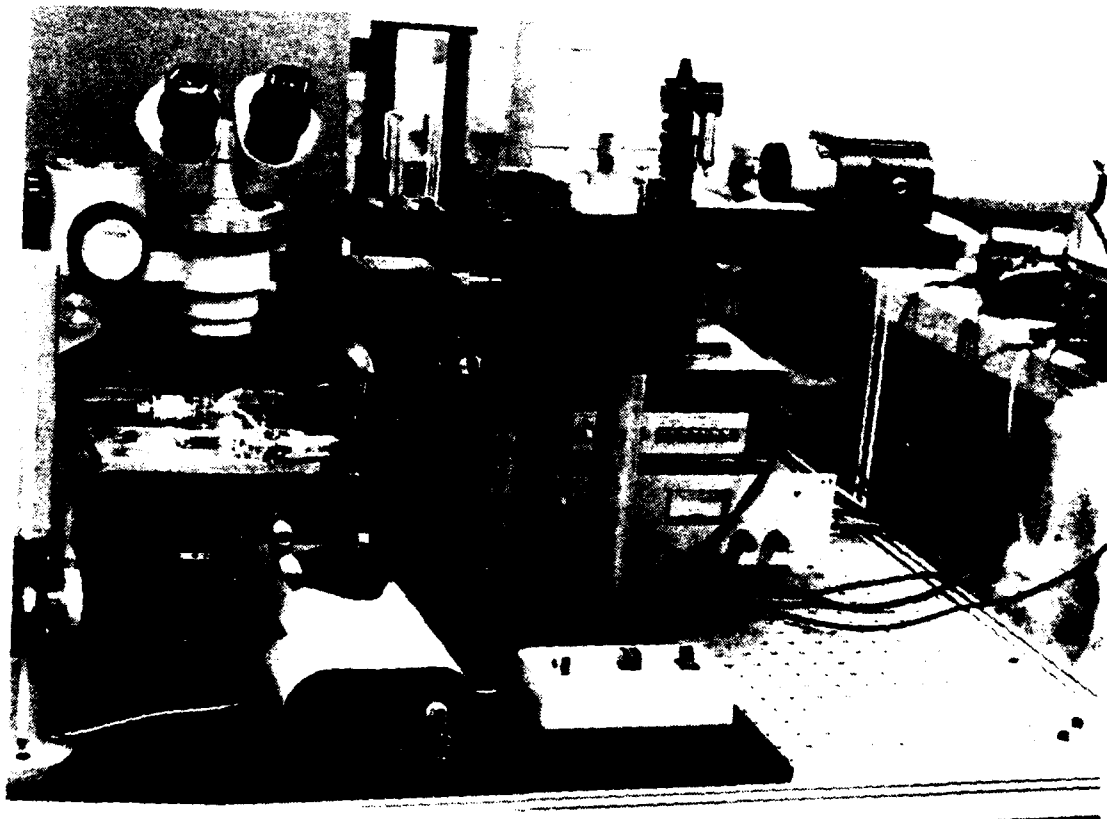
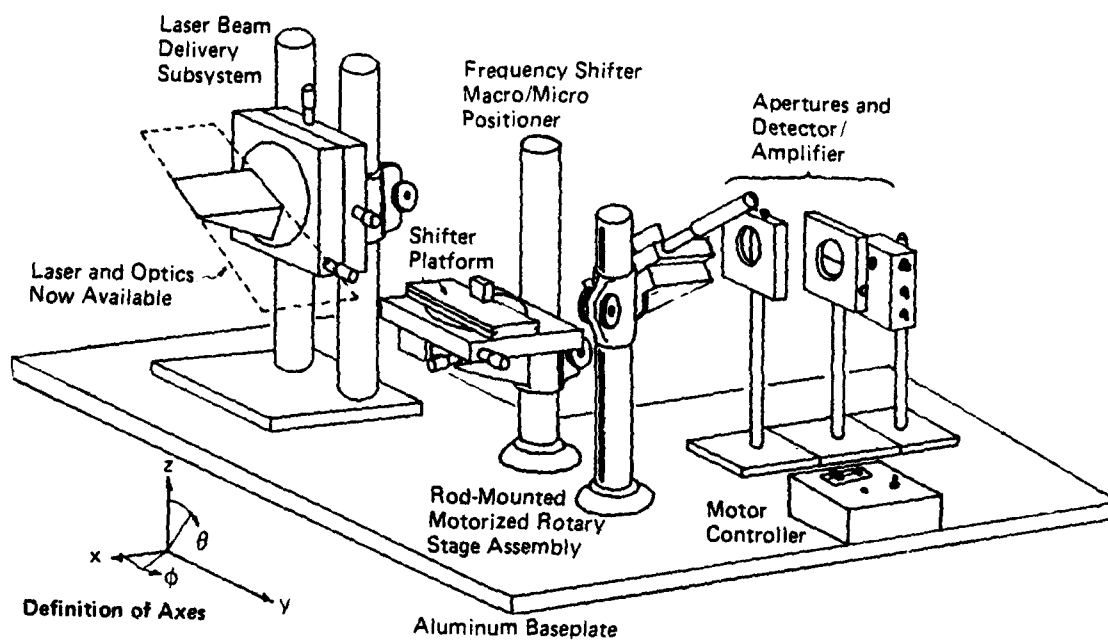
21227-12

Figure 6-6. Collapsed Lip (Tableclothing)

The first frequency shifters produced at NRTC had IDTs composed of two metal layers:  $\sim 200\text{\AA}$  chromium in contact with the LN waveguide, and  $\sim 800\text{\AA}$  gold in contact with the chromium. The first frequency shifters produced at PPD had a single layer of  $\sim 900\text{\AA}$  aluminum in contact with the LN waveguides. The aluminum was deposited by RF sputter deposition from an apertured target. After deposition, the coated waveguides are immersed in clean, room temperature acetone and ultrasonically agitated for five minutes. Initial attempts at this liftoff procedure failed due to poor aluminum adhesion to the waveguide surface, partially because of photoresist scumming and partly because of the fairly low adhesion energy displayed by aluminum on glassy surfaces. A working frequency shifter was produced by extending the development time by a few seconds to reduce scumming; the shifter failed after approximately two hours of operation due to low adhesion. Future frequency shifters at PPD will possess IDTs composed of  $\sim 200\text{\AA}$  chromium in contact with the waveguide, and  $\sim 800\text{\AA}$  aluminum or gold in contact with the chromium. Scumming problems will be eliminated by short-term insertion of the resist-coated waveguide in a new plasma asher. We will also investigate the application of  $\text{SiO}_2$  buffer layers  $\sim 2000\text{\AA}$  thick between the waveguide and the IDTs, and final protective magnesium fluoride layers over the IDTs to reduce the probability of handling-related failures.

Proper testing of a SAW frequency shifter involves the exploration of the electrical, optical, and spatial interactions taking place within the device. To this end we have developed high-frequency electronic and optical detectors, and have assembled a precision mechanical setup (shown in figure 6-7) capable of facilitating both end-fire and prism input/output coupling methods.

The beam delivery pod was made large enough to hold a small commercial two-mode laser (or in-house-built single-mode scanning laser) and any necessary beam-shaping and polarizing optics, thus minimizing alignment-related optical problems. The pod is capable of precise movement in the vertical and horizontal (x) to allow focal-point positioning, and of precise azimuthal angle setting for synchronous angle search. The SAW frequency shifter pod is large enough to serve as an optics and RF detector mount/ground plane and is capable of precise movement in the horizontal (y) and of precise longitudinal angle setting for Bragg angle studies. Waveguide output is reflected from a scanning mirror through apertures into either a high-speed optical detector for beat-detection of harmonics or into a scanning Fabry-Perot interferometer for out-right shift frequency measurement. The scanning mirror allows the spatial intensity or frequency distributions to be found without moving the detector. All mechanical components are mounted on a common aluminum baseplate for stability and compactness.

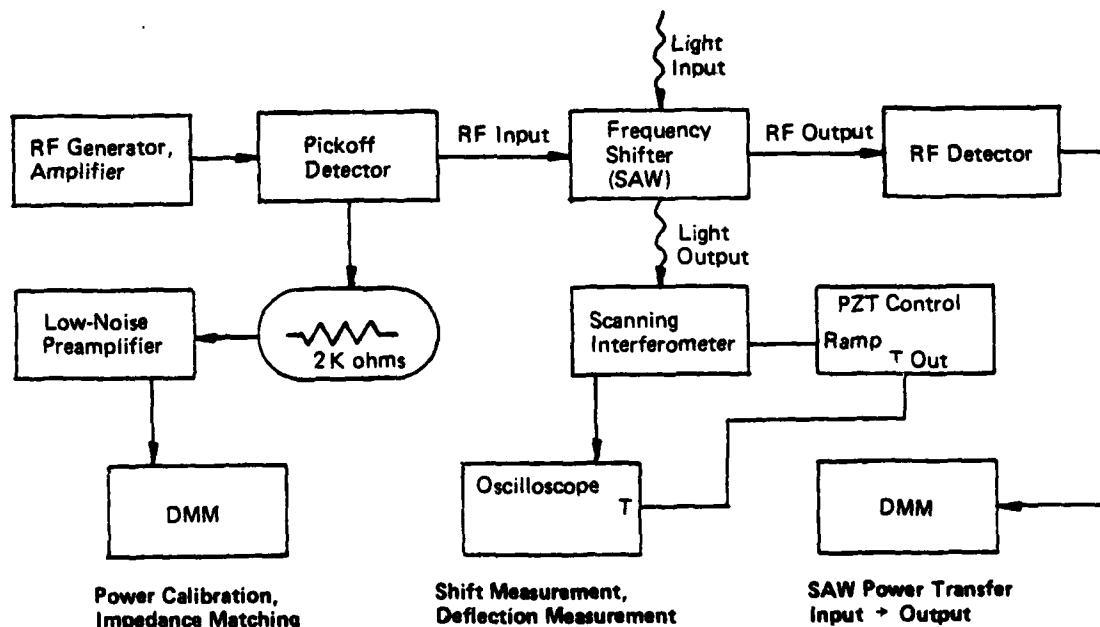


21227-18

Figure 6-7. Frequency Shifter Evaluation Assembly

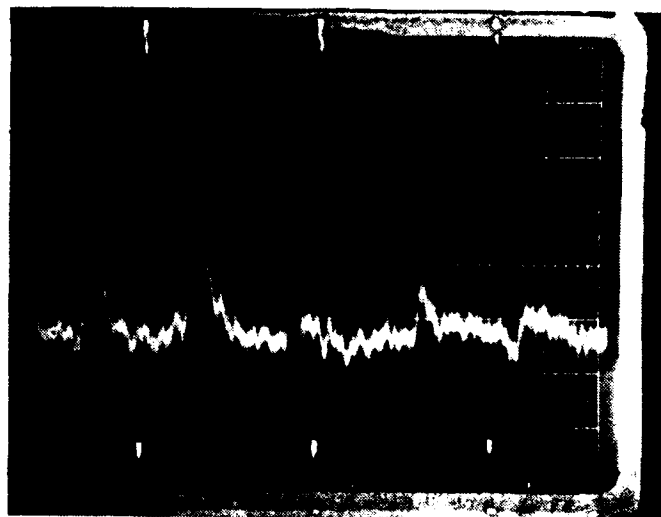
RF signal generation is performed by a commercial unit capable of RMS voltages up to 1 V into 50 ohm coaxial over a 19 MHz to 520 MHz bandwidth with harmonic distortion at >20 dB below the carrier level. The signal may be AM or FM demodulated for phase-locked loop detection. The output signal is further amplified 11.8 dB by a hybrid RF amplifier to boost power levels in the event of impedance mismatch. A commercial pickoff type directional power meter with very small insertion loss is inserted between the hybrid amp output and frequency shifter input, enabling frequency-shifter input power estimation based upon forward and reflected power data. These data also ease the task of experimental impedance matching. For studying the SAW propagation, a terminating RF detector is placed across the output IDTs of the SAW (figure 6-8). The RF is fed directly to the transducer pads in the lithium niobate crystal.

The first frequency shifter test incorporated end-fire input coupling with prism output coupling and with no aperturing in front of the scanning interferometer. Impedance matching was not performed initially; about 2/3 of the applied RF power was reflected at the IDT. Power levels for 60 percent conversion efficiency were ~40 mw and were calculated from corrected reflection/transmission data. Optical alignment was fair but not optimized. It was found that the resonant frequency of the input IDTs was 210 MHz  $\pm$  3 percent (210  $\pm$  6 MHz). A photograph of the scanning interferometer output is shown in figure 6-9. Second-order shift was not observed. After approximately two hours of operation the shifter failed due to poor IDT adhesion to the LN waveguide. This first working shifter verified successful photolithography, liftoff, and testing and established the capability of frequency shifter fabrication at PPD.



21227-21

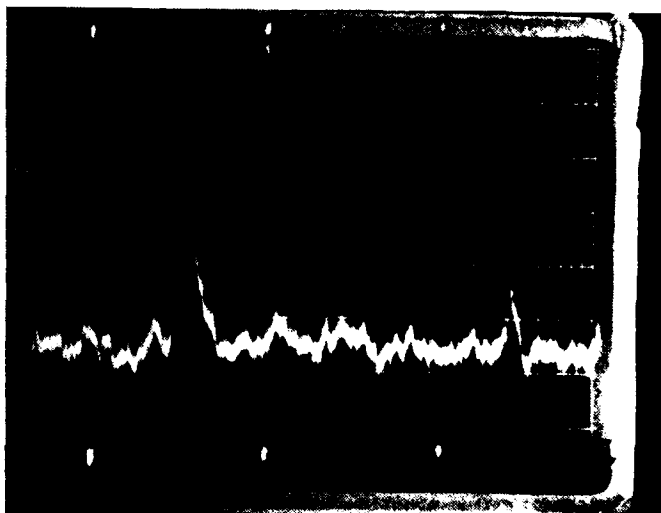
Figure 6-8. SAW Test Block Diagram



207 MHz

FSI 9/16/82

200 MHz Shifted Beam. Unshifted residue is the smaller peak at left of center. Conversion efficiency was approximately 60% at 40 mw input RF power.



No Shift

FSI 9/16/82

Unshifted Beam. Note high noise levels due to optical misalignment.

21227-13

Figure 6-9. Scanning Interferometer Output

## Section VII

### CONCLUSIONS AND RECOMMENDATIONS

The work carried out under this contract provides much of the technology base necessary for assembling a prototype of the micro-optic gyro. It was demonstrated that PPD has the capability to fabricate frequency shifters and horn waveguides suitable for the micro-optic gyro breadboard.

It was not possible to complete the final task of integrating the frequency shifters and polymer waveguides and resonators due to the failure to etch a satisfactory step in the lithium niobate. The etching is a critical step in the integration approach selected. The difficulties are not fundamental. It has been done in other laboratories, but it does involve extensive experimentation with the sputter etch unit design and process parameters.

The assembly of the optical portion of the micro-optic gyro using integration techniques developed during this program will continue. Because of the difficulty with the etching process, an alternate approach not requiring etching will be initiated while the etching capability is developed.

The experience gained on this program in fabricating thin-film frequency shifters led to a redesign of the photolithography area and an expansion of the fabrication facilities using PPD capital funds. The new laboratory and associated assembly clean rooms provide a capability not only to make thin-film frequency shifters in sufficient quantities for prototype gyro assembly, but also to develop alternate components and approaches. Thus, while the frequency shifter-resonator integration task has slipped into 1983, the planned prototype gyro fabrication remains scheduled for late 1983.

## REFERENCES

1. A. Lawrence, J. Segre, "Studies on the Micro-Optic Gyro," Final Report on Contract N60530-78-C-0014, Naval Weapons Center, China Lake, CA 26 May 1978.
2. J. R. Haavisto, A. Lawrence, "Micro-Optic Gyro Technology," TR-RG-CR-80-2, Final Report on Contract DAAK-40-79-C-0052, December 1979.
3. A. W. Lawrence, J. R. Haavisto, G. A. Pajer, "Micro-Optic Gyro Technology, TR-RG-CR-81-1, Final Report on Contract DAAK-40-79-C-0235, November 1980.
4. J. Haavisto and G. Pajer, Opt. Lett 5, 510 (1980).
5. W. S. C. Chang, et al, "Integrated Optics," p. 313 of "Laser Applications," Vol. II, M. Ross Ed., Academic Press, New York (1974).
6. W. K. Burns, A.F. Milton, and A. B. Lee, Appl. Phys. Lett, 30, 28 (1977).
7. A. F. Milton and W. K. Burns, IEEE JQE, QE-13, 828 (1977).
8. B. L. Sopori, et al, Appl. Optics, 19, 790 (1980).

## Appendix A

### TAPERED HORN EXPERIMENT

This simple experiment proved useful and of some interest in illustrating the guiding properties of a horn whose effective index varied not only transverse to the direction of propagation, but parallel to it as well. It was also quite illustrative in showing how the fabrication geometry formed the final horn structure as nonlinear in width and height as functions of position along the horn. Imprecision in measurement does not allow experimental verification of theory regarding  $n$  as a function of position, nor do the measurements allow us to take a detailed look at the optical properties of the structure in the vicinity of the horn waist. At the very least, this venture showed what level of measurement precision must be attained to observe the mode structure within future parabolic horns. Further correlation of the observations of this tapered horn and future horns will undoubtedly be limited due to differences in geometric and refractive index structures.

A horn waveguide was produced in a thin ( $\sim 3 \mu\text{m}$ ) film of PMMA atop a quartz disk normally used in passive ring resonator experiments. While the guides employed in the resonators have parallel walls on the order of  $5 \mu\text{m}$  apart, this particular waveguide had wall spacing as a function of position along the waveguide, and resembled roughly what is known as a tapered waveguide. The tapered horn, as we will call it, was produced by placing the disk/PMMA film at a large angle to the axis of the UV laser's focused beam. It was believed before the experiment and confirmed afterward that this angular displacement would produce a tapered horn possessing a waist whose size would be of the same order of magnitude of the focused beam waist - roughly  $5 \mu\text{m}$ . The angle of inclination was  $72.5^\circ$  with respect to the beam.

Optical observation and physical examination of the tapered guide have been undertaken and will be described below. Analysis of the observation was carried out - in the spirit of good approximation - to render some idea of how the index change in the film varied with position along the horn axis.

#### PHYSICAL DESCRIPTION

Upon examination of the tapered horn under the Zeiss interferometric microscope, it was found that the horn was not a simple taper having as its cross-section a linear function of position along the axis. Inspection of figure A-1 would suggest that  $w(x)$  might be approximated by

$$w(x) = 2 [C - A \exp - (x^2/b^2)]$$

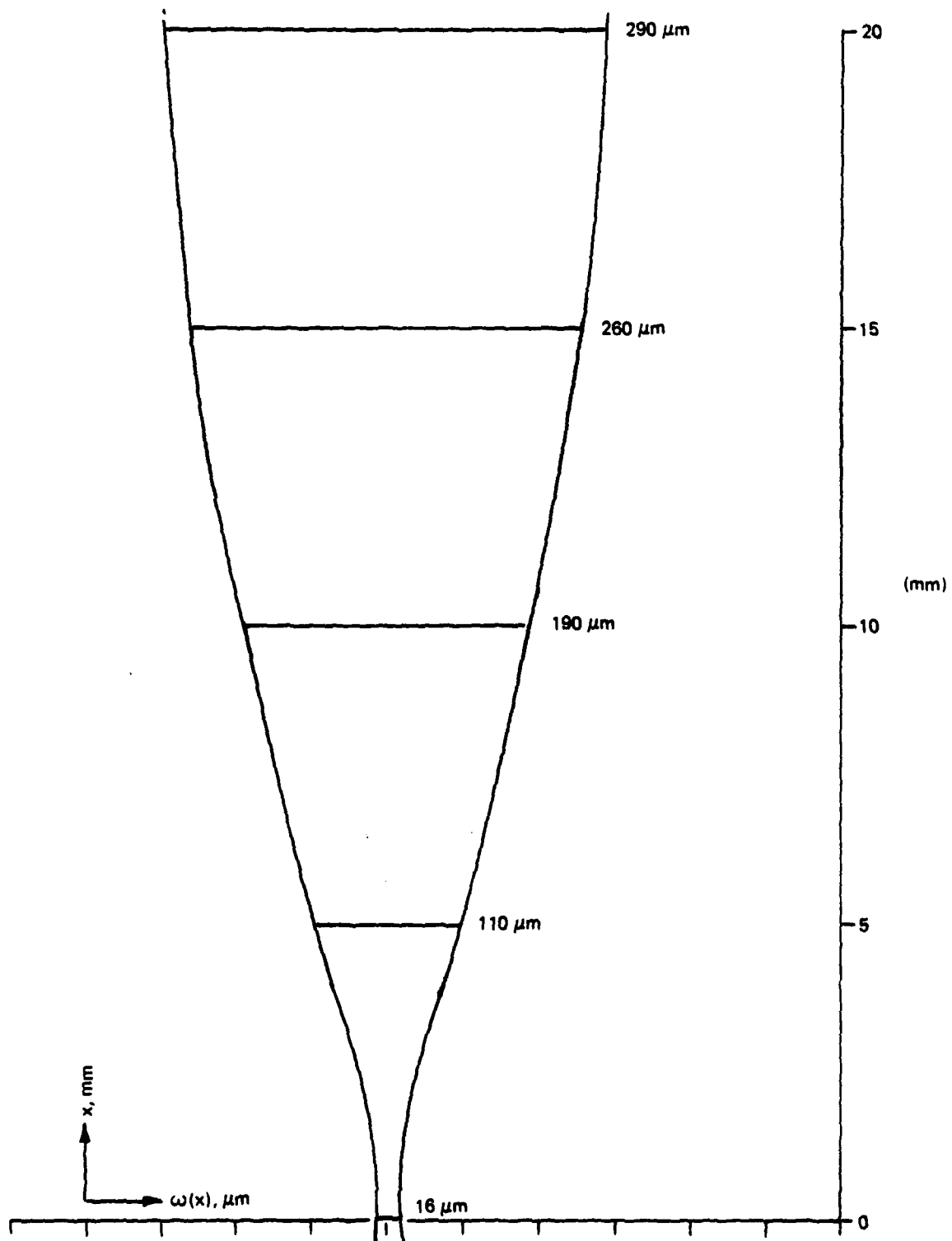
where

$$C = 150 \mu\text{m}$$

$$A = 142 \mu\text{m}$$

$$b = 3000 \mu\text{m}$$





21227-31

Figure A-1. Horn Width vs  $X$  (note difference in scales)

An exact equation would take into account the beam profile as a function of height, the angle between the disk normal and the beam axis, and the responsivity of the photolocking film. The horn possessed bilateral symmetry along two axes: the axis parallel to the x-direction (defined in figure A-1) and bisecting the width,  $w(x)$ ; the axis perpendicular to  $x$  in the plane of the figure and cutting the waist  $w(0)$ . These symmetries are not surprising given even the crude nature of the fabrication process. Indeed nothing about the  $w(x)$  of the tapered horn is very surprising; however, what is surprising is the suggestion of some photosaturation phenomenon in PMMA by the height function  $h(x)$  along the length of the horn. See figure A-2.

The question arises as to whether this deviation is due to photosaturation or fabrication geometry. One might think initially that, given constant stage speed (stage speed determines the amount of energy deposited on the PMMA film per pass), the largest amount of power, and therefore density change would occur at the intersection of the beam waist and the PMMA film. So, then we expect to see maximum guide height at the guide waist.

This is not the case, as figure A-2 shows. Maximum guide height occurs at approximately 5 mm from guide waist, and is roughly 36 percent larger than the height at the guide waist.

Suppose further that photolocking is a function of density change. We can only observe the volume change under  $\Delta x$  along the surface of the film and make various guesses regarding the photolocking that has been induced within that small volume. Since  $\Delta V \approx A(x) \Delta x$ , we can bypass the complicated volume calculation and look at any  $A(x)$  in  $dx$  to surmise the volume about  $x_0$ . Approximating  $h(x)$  the height of the guide as being of gaussian form across the guide, we have

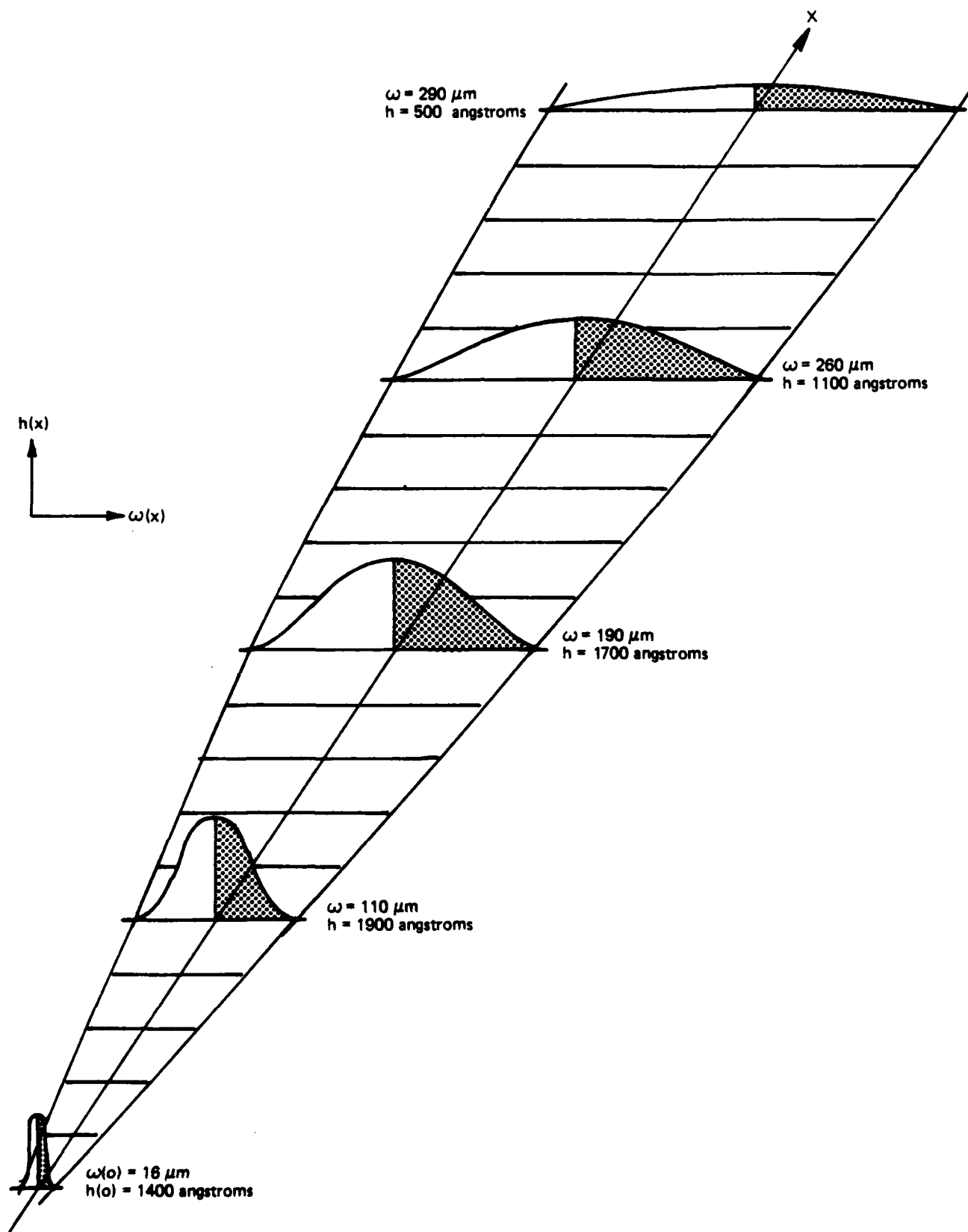
$$A(x) = [h(x) w(x) \sqrt{\pi}] / 2$$

Calculating  $A(x)$  and plotting vs  $x$  shows that  $A(x)$  possesses a maximum near  $x = 2.0$  mm. See figure A-3.

To determine whether this observed behavior of  $h(x)$  is a natural consequence of the fabrication geometry, it is necessary to consider the beam shape as changing along the  $x$ -direction; the total volume change at any point  $x_0$  will be a result of an integration of the beam strength as it changes near  $x_0$ . As an example, in the sketch below, a beam of constant width passes over the point  $x_0$  for some time interval  $\Delta t$ .

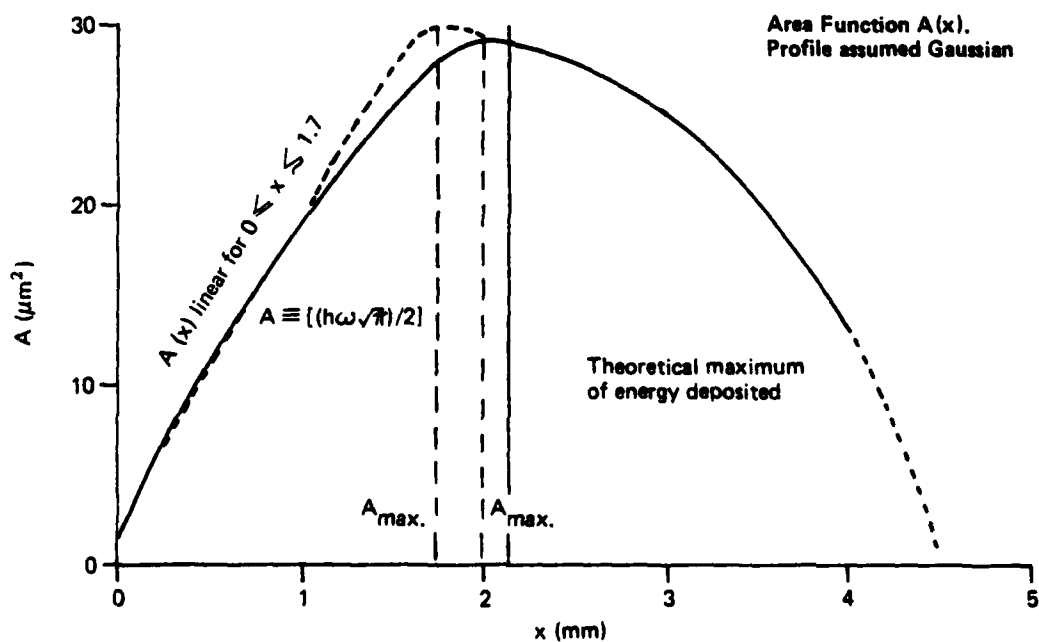
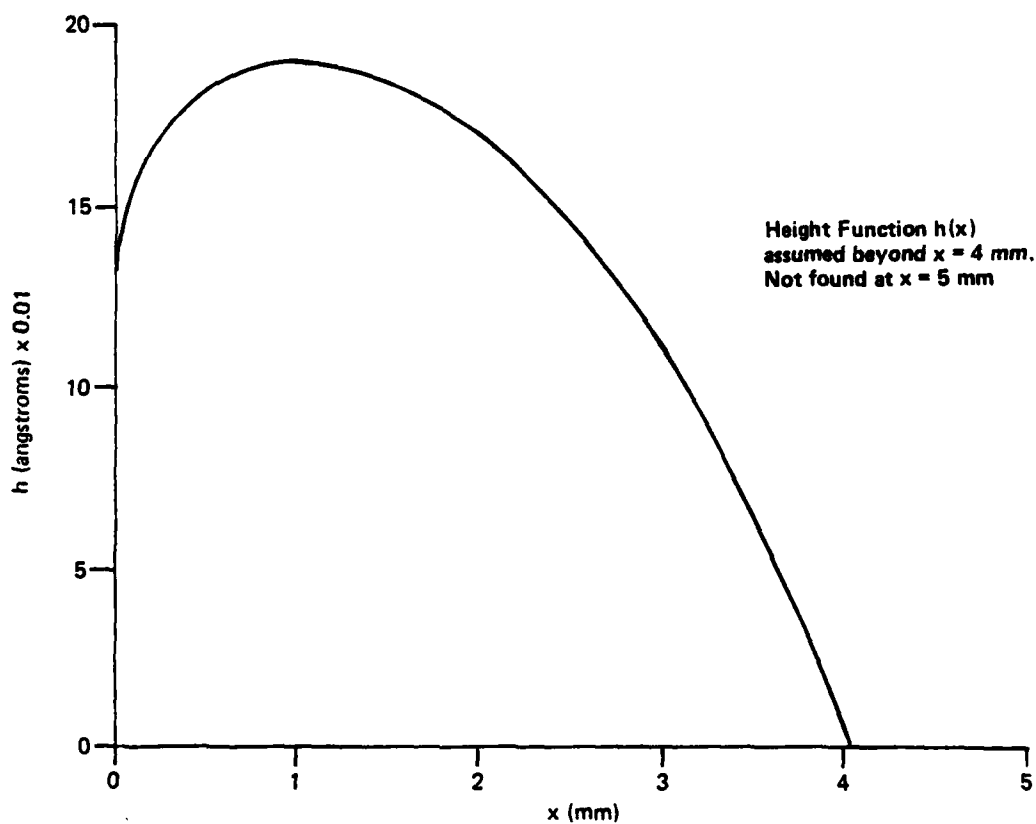
The total energy left at  $x_0$  then is

$$E \approx P \Delta t \approx \int I_2 dx, \text{ where } I \approx A \exp [-(x^2/a^2)]$$



21227-32

Figure A-2. Sample Profiles Taken 5 mm Apart, Beginning at Beam Waist,  $\omega(0)$



21227-33

Figure A-3. Height Function and Area Function

Then consider if the width of the beam is increasing as it passes over  $x_0$ . The beam is over  $x_0$  for a longer period of time, but the beam intensity is spread out over a much larger area. Since the time is proportional to the changing width and the intensity is proportional to the inverse of the changing width squared, we might say that the change in energy is roughly:

$$\Delta E \propto [\Delta (1/W^2)] \rightarrow [2X/(B^2 w^3)]; \quad [(d^2E)/(dx^2)] \propto (2A/b^2)$$

$$\{(1/W^2) + [(2X^2)/(W^2 b^2)]\}$$

A more commonsense approach would state that where the rate of change of the beam width is at a maximum, that is where the beam leaves the most energy, since it is at that point the beam seems delayed the longest. The inflection point of the gaussian described earlier is at  $x' = (b/\sqrt{2}) = 2.12$  mm. This is in fair agreement with the area maximum  $A(x)$  maximum shown in figure A-3. A computer program will be employed at some later time to find a more accurate number for  $x$ .

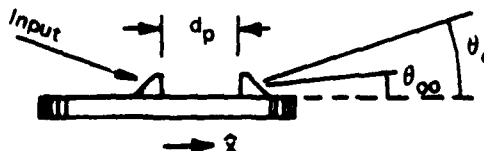
We may now tentatively conclude that the variation of density change with  $x$  is a result of fabrication geometry only, and has nothing to do with any photosaturation phenomena.

#### OPTICAL DESCRIPTION

The more interesting aspects of the tapered horn include what the horn does to the light being guided within it. Besides wanting to know the physical dimension of the waveguide, it is useful to know how the refractive index varies over those dimensions, and eventually to realize the mode structure the horn is capable of supporting. To this end we guided light within the horn and attempted to measure the synchronous angles for specific modes as a function of position along the length of the guide. The modes observed quantitatively were described by  $\theta_0(x)$ ,  $\theta_{00}(x)$ ; in all measurements, the beam was aligned colinearly with the axis of the tapered horn.

#### Procedure

The input prism was placed and fixed with its coupling region very near the "middle" of the disk (figure A-4). Without having actually seen the guide beforehand using the Zeiss, it was believed that the prism was placed such that a good deal of energy would be coupled into the very wide part of the horn. The following data is presented using  $d_p$ , the prism spacing, as the variable. For all observations, the input angle of beam remained the same. The input angle was adjusted at the outset such that for  $d_p$  at maximum (about 35 mm) the zeroth planar and its associated zeroth channel mode were visually optimized with regard to line sharpness and intensity.



21227-34

Figure A-4. Input Prism Coupling Region

Table A-I

## Refractive Index Variations over Dimensions

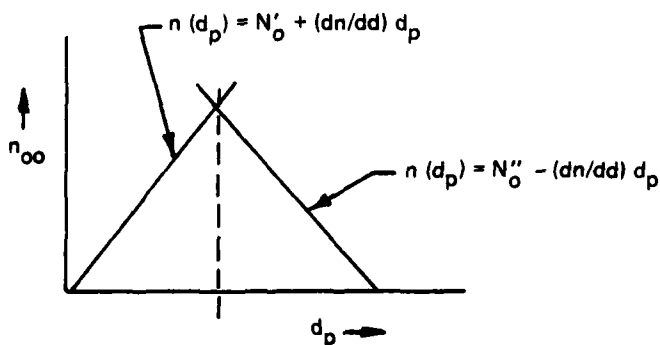
$d_p$	Measured $\theta$ calculated from $\tan^{-1}$ (up/over)	$\Delta\theta$	Corrected $\Delta\theta$ Using $\theta_0 = 11.401$	Comments
35 mm	$\theta_0 = 11.313$ $\theta_{00} = 11.712$	$\Delta_1 = 0.399$	$\Delta'_1 = 0.311$	Lots of modes visible if the beam is moved off axis. Lots of power. Channel signature $\approx 35$ mm wide
28 mm	$\theta_0 = 11.354$ $\theta_{00} = 11.982$	$\Delta_2 = 0.628$	$\Delta'_2 = 0.581$	Still lots of modes. Can now isolate channel signature, about 50 mm wide.
20 mm	$\theta_0 = 11.443$ $\theta_{00} = 12.196$	$\Delta_3 = 0.753$	$\Delta'_3 = 0.795$	Only five channel modes visible. Even more power. Can't isolate zeroth channel signature $\approx 100$ mm wide. Others always present.
17.5 mm	$\theta_0 = 11.448$ $\theta_{00} = 12.232$	$\Delta_4 = 0.784$	$\Delta'_4 = 0.831$	Reminded of observation at 35 mm (above). Cannot isolate zeroth channel $\approx 50$ mm wide. <u>Fifteenth</u> channel mode very clear.
15 mm	$\theta_0 = 11.420$ $\theta_{00} = 12.137$	$\Delta_5 = 0.717$	$\Delta'_5 = 0.736$	Cannot isolate zeroth channel to measure it. However, <u>thirtieth</u> channel quite clear and $\approx 250$ mm wide.
10 mm	$\theta_0 = 11.430$ $\theta_{00} = 11.883$	$\Delta_6 = 0.453$	$\Delta'_6 = 0.482$	Zeroth channel mixed. Probably about 30 to 45 mm across. The highest order channel mode appears continuous across its width.

Treating all the points as symmetric about some  $d_p$  at the beam waist, we can separate the points into a set of two lines having equal slopes (but of opposite sign) (see figure A-5). Also treating the first point at  $d_p = 10$  as a fluke ( $\Delta n/\Delta d$  between it and the closest point is about twice the value of  $\Delta n/\Delta d$  elsewhere), we may find that an "average" slope of  $dn/dd = 0.0001603$  will satisfy the equations with  $N'_0 = 1.49229$ ,  $N''_0 = 1.49804$ , the parameters which fit the points optimally. The corrected data point is shown with the measured value in parentheses (see table A-II and figure A-6). Solving the equations for  $d_p$  gives the value for the beam waist,  $d_p = 17.96$  mm;  $n$  (waist) = 1.49517, and is probably larger than the true value due to the linear approximation. Remember that by Kogelnik,  $\Delta n$  is double valued with respect to  $W$ .

Table A-II

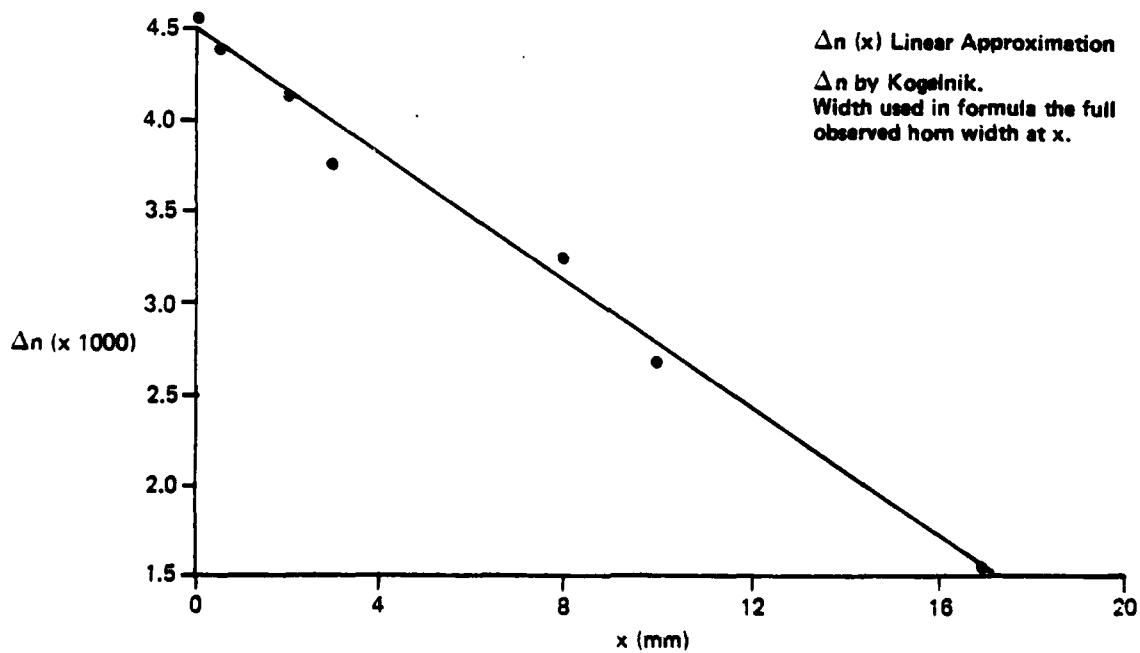
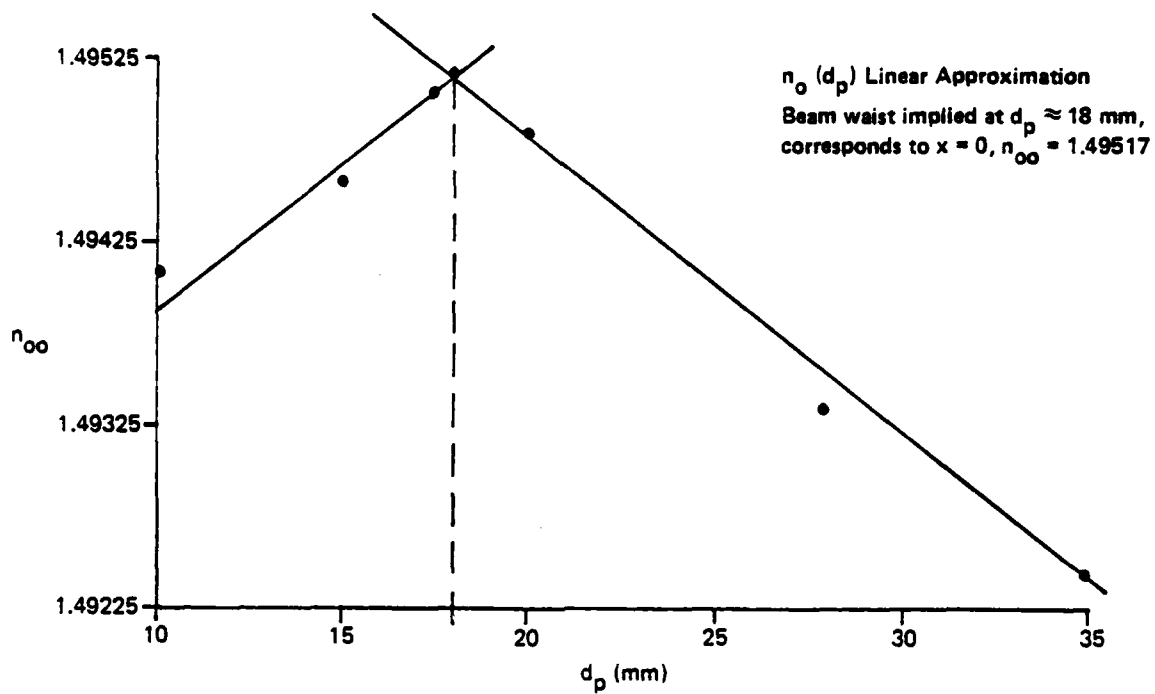
$$\theta'_0 = 11.401 \quad \sigma_{n-1} = 0.055 \quad N'_0 = 1.49088 \quad \Delta n \text{ by Kogelnik}$$

$d_p$	$n_{00}(d_p)$	$n(d_p) \times 1000$
10	1.49408 (1.49305)	3.18 - 3.22 (2.15 - 2.19)
15	1.49456	3.62 - 3.76
17.5	1.49503	3.93 - 4.40
20	1.49485	3.87 - 4.12
28	1.49353	2.64 - 2.67
35	1.49244	1.55 - 1.57
Waist	1.49517	4.07 - 4.55



21227-35

Figure A-5. Linear Approximation Approach



21227-36

Figure A-6. Details of Linear Approximations

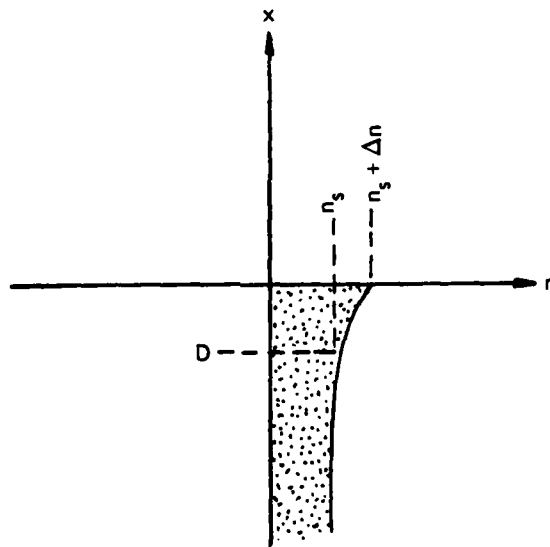


## Appendix B

### DIFFUSED WAVEGUIDE PARAMETERS

The purpose of this appendix is to outline a technique for determining the parameters of titanium in-diffused lithium niobate waveguides using the measured waveguiding properties. We present an example of the technique using the data for three waveguides fabricated at PPD.

The parameters of a diffused waveguide which determine the waveguiding properties are the amount of induced index change at the surface ( $\Delta n$ ) and the diffusion depth ( $D$ ). The former is dependent on the concentration of diffused ions (Titanium) at the surface of the crystal substrate ( $\text{LiNbO}_3$ ) and the latter is the depth below the surface equivalent to the  $1/e^2$  point (figure B-1). The actual distribution of ions below the surface may be exponential, Gaussian, erf, or some other function depending on the diffusion parameters and ion kinetics. Our purpose here is to establish a convenient analytically based procedure which will allow us to determine the waveguide parameters ( $\Delta n$ ,  $D$ ) from the observed waveguide properties.



21227-37

Figure B-1. Waveguide Profile

The first step in this procedure is to establish an acceptable form for the diffusion profile. The accepted profile for the diffusion process we use is Gaussian.<sup>1</sup> Here the index of refraction varies as

$$n(x) = n_s + \Delta n e^{-(x/D)^2} \quad x \leq 0$$

Where  $n_s$  is the index of lithium niobate (2.20) and  $x$  is the depth ( $x = 0$  at the surface). With this form, the wave equation must be solved numerically or approximated using the WKB approximation.<sup>(2,5)</sup> The latter is an integral solution, and generally requires numerical integration. There appears no convenient way to use this profile in a straightforward manner. Our approach is to assume the index distribution can be approximately described by an exponential function

$$n(x) = n_s + \Delta n e^{-|x|/D} \quad x \leq 0$$

In this case, the wave equation can be solved analytically.<sup>(3)</sup> The field distribution of the guided modes are Bessel functions ( $J_v(\alpha x)$ ) in form where both  $v$  and  $\alpha$  are functions of the waveguide parameters ( $\Delta n$ ,  $D$ ).

The waveguiding is characterized by modal propagation constants ( $\beta_i$ ) which are discrete values related to the propagation velocity of the guided wave. This propagation constant is determined by measuring the synchronous angle required to excite the guided wave. Each guided mode will have a specific propagation constant associated with it. The propagation constants are related to the order of the Bessel function ( $v$ ) when the boundary conditions are enforced. It has been shown<sup>(3)</sup> this is approximately at the zeros of the Bessel function; i.e.,

$$J_v(\alpha x_0) = 0$$

Thus, if we know  $\Delta n$  and  $D$ , the equation is

$$J_v(\beta_i)(\xi) = 0$$

where  $\xi$  is a constant. We can use the measured values of  $\beta_i$  to invert this procedure and calculate  $\Delta n$  and  $D$ . Now we require two equations; i.e., propagation constants for two modes of the same waveguide to solve for  $\Delta n$  and  $D$ :

$$J_{v_1}^{(\beta_1)}(\xi(\Delta n, D)) = 0$$

$$J_{v_2}^{(\beta_2)}(\xi(\Delta n, D)) = 0$$

On three mode guides, this results in three values for  $\Delta n$  and  $D$  from which a mean and standard deviation can be taken. On single-mode guides, either  $\Delta n$  or  $D$  has to be given to calculate the other.

The waveguides analyzed included two three-mode waveguides of similar diffusion parameters and a single-mode guide diffused for one-quarter of the time. This should result in a reduction of one-half in  $\Delta n$  and  $D$ . Our approach was to find a suitable scaling of  $\Delta n$  and  $D$  for the single-mode case.

The propagation constants were calculated using:(4)

$$B_{ijk} = \tilde{N}_i = \sin \theta_i \cos \epsilon + (\sqrt{n_p^2 - \sin^2 \theta_i} \sin \epsilon)$$

where

$\epsilon$  = prism angle ( $47.86^\circ$ )

$n_p$  = index of prism (2.903)

$\theta_i$  = synchronous angle for mod i

$k$  = free space propagation constant ( $2\pi/\lambda$ )

The setup is shown in figure B-2.



21227-38

Figure B-2. Evaluation Setup

The explicit form of the Bessel function is

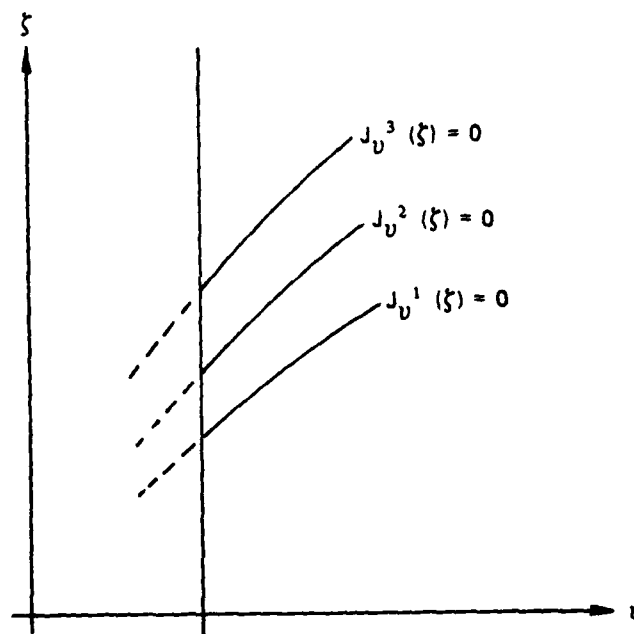
$$J_v^i(\xi) = 0$$

$$v = 2Dk \sqrt{\tilde{N}_i^2 - n^2}$$

$$\xi = 2Dk \sqrt{2n\Delta n}$$

where  $n$  = substrate index (2.20).

The zeros of the Bessel function are given graphically as a function of  $v$  and  $\xi$  (see figure B-3).



21227-40

Figure B-3. Bessel Function Zeros

Only the curves for the three lowest modes are shown. By combining equation (8) for mode  $i$  and mode  $j$ , we can eliminate  $D$  and solve for  $\Delta n$ . We obtain

$$\Delta n = \left( \frac{z_j a_i \sqrt{\tilde{N}_i^2 - n^2} - z_i a_j \sqrt{\tilde{N}_j^2 - n^2}}{(z_j - z_i) \sqrt{2n}} \right)^2$$

where the curves in figure B-3 are approximately given by a straight line

$$a(i) = z_i + a_i v_i$$

Thus  $z_1$  is the  $z$ -intercept and  $a_1$  the slope for the  $i$ th mode. From the graph

$z_1 = 2.42$	$a_1 = 1.54$
$z_2 = 5.55$	$a_2 = 1.56$
$z_3 = 8.68$	$a_3 = 1.59$

The synchronous angles yield the effective indices (propagation constants/k)

Sample 3  $\tilde{N}_1 = 2.2073$

$\tilde{N}_2 = 2.2045$

$\tilde{N}_3 = 2.2007$

Sample 4  $\tilde{N}_1 = 2.2130$

$\tilde{N}_2 = 2.2045$

$\tilde{N}_3 = 2.2007$

Sample 1  $\tilde{N}_1 = 2.2035$

Calculating  $\Delta n$  yields

Sample 4  $\Delta n = 0.032 \pm 0.010$

Sample 3  $\Delta n = 0.050 \pm 0.01$

The diffusion depth can be calculated from

$$D_i = \frac{Z_i}{2k [\sqrt{2n\Delta n} - a_i \sqrt{\tilde{N}_i^2 - n^2}]}$$

We use  $\Delta n$  data from each sample which yields

Sample 3  $\bar{d} = 1.15 \pm 0.03 \mu$

Sample 4  $\bar{d} = 1.15 \pm 0.03 \mu$

Using  $D = 0.6 \bar{d}$  ( $0.69 \mu$ ) produces  $\Delta n = 0.06 \Delta n$  where  $\Delta n = 0.050$ ; i.e., the  $\Delta n$  calculated for Sample 4. Similarly, using  $\Delta n$  from Sample 3 we calculate that for  $1/2 \Delta n$  the diffusion depth is  $1/2 D$ . The specific figures are

$D = 1/2 \bar{d} = 0.59$

$\Delta n = 0.017 = 1/2 \Delta n (\Delta n = 0.032)$

#### REFERENCES (Appendix B)

1. G. B. Hocker and W. K. Burns, IEEE, JQE-11, 270 (1975).
2. -----, Appl. Opt. 16, 113 (1977).
3. E. Conwell, App. Phys. Lett., 23, 328 (1973).
4. R. Ulrich and R. Torge, Appl. Opt., 12, 2901 (1973).

DATE  
FILMED  
8